

Full Length Article



A scalable well-balanced numerical scheme for the simulation of fast landslides with efficient time stepping

Federico Gatti ^{a,b,*}, Carlo de Falco ^a, Simona Perotto ^a, Luca Formaggia ^a

^a MOX – Modelling and Scientific Computing, Department of Mathematics, Politecnico di Milano, Milan, Italy

^b Consiglio Nazionale delle Ricerche - Istituto di Matematica Applicata e Tecnologie Informatiche “E. Magenes” (CNR-IMATI), Pavia, Italy

ARTICLE INFO

Keywords:

Taylor-Galerkin scheme
Depth-integrated models
Implicit-explicit Runge-Kutta-Chebyshev scheme
C-property
Path-conservative methods
Parallel simulations

ABSTRACT

We consider a single-phase depth-averaged model for the numerical simulation of fast-moving landslides with the goal of constructing a well-balanced, yet scalable and efficient, second-order time-stepping algorithm. We apply a Strang splitting approach to distinguish between parabolic and hyperbolic problems. For the parabolic contribution, we adopt a second-order Implicit-Explicit Runge-Kutta-Chebyshev scheme, while we use a two-stage Taylor discretization combined with a path-conservative strategy, to deal with the purely hyperbolic contribution. The proposed strategy allows to decouple hyperbolic from parabolic-reaction stiff contributions resulting in an overall well-balanced scheme subject just to stability restrictions of the hyperbolic term. The spatial discretization we adopt is based on a standard finite element method, associated with a hierarchically refined Cartesian grid. After providing numerical evidence of the well-balancing property, we demonstrate the capability of the proposed approach to select time steps larger than the ones adopted by a classical Taylor-Galerkin scheme. Finally, we provide some meaningful scaling results on ideal and realistic scenarios.

1. Introduction

The two-step Taylor-Galerkin (TG2) method, introduced in [1–3], has been recently applied to the simulation of fast landslides [4,5]. TG2 coincides with an explicit scheme. Consequently, it can be efficiently implemented in a parallel framework, yet it could require a too restrictive time step compared to the landslide run-out time scale. This is due to the stiffness of the parabolic part and of the source characterizing the landslide model.

In this paper, we propose a new method that enables to use of larger time steps than the explicit TG2 scheme while preserving the data locality property, which represents a key aspect for the implementation of a highly scalable code (see, e.g., [6]). The new method merges the second order Implicit–Explicit Runge–Kutta–Chebyshev (IMEX-RKC) finite element scheme on hierarchical quadtree meshes with a TG2 approach enriched by a path-conservative (PC) procedure (namely, a TG2-PC approximation), by resorting to a Strang splitting scheme [7,8]. This choice allows us to integrate non-conservative products to guarantee

* Corresponding author.

E-mail addresses: federico.gatti@polimi.it, federico.gatti@imati.cnr.it (F. Gatti), carlo.defalco@polimi.it (C. de Falco), simona.perotto@polimi.it (S. Perotto), luca.formaggia@polimi.it (L. Formaggia).

<https://doi.org/10.1016/j.amc.2023.128525>

Received 21 February 2023; Received in revised form 25 October 2023; Accepted 26 December 2023

0096-3003/© 2023 The Author(s). Published by Elsevier Inc. This is an open access article under the CC BY-NC-ND license (<http://creativecommons.org/licenses/by-nc-nd/4.0/>).

a well-balanced property. In other words, we approximate the diffusion-reaction contribution with a finite element IMEX-RKC scheme and the transport term with the TG2-PC method. The complete scheme will be referred to as Split IMEX-RKC TG2-PC method.

Concerning PC methods, the basic theory has been formalized by G. Dal Maso, P.C. Lefloch and F. Murat [9] on weak solutions to hyperbolic partial differential equations with non-conservative products, and successively developed by C. Parés, M.J. Castro and co-workers in the framework of a finite-volume discretization [10–18]. In particular, in the approximation of shallow water equations, it has been demonstrated that PC methods guarantee a well-balanced numerical scheme [19,20]. The PC strategy has already been successfully employed in the literature in the context of a discontinuous Galerkin (DG) spatial discretization, see [21,22]. On the contrary, to the authors' knowledge, the PC scheme has never been adopted in a continuous finite element setting. In the verification phase, we provide numerical evidence of the capability of PC schemes to satisfy the well-balance property also when dealing with a continuous finite element approximation.

Regarding the IMEX-RKC method, the approach was introduced in [23] as an extension of the Runge–Kutta–Chebyshev (RKC) method first proposed in [24], and successfully used in reaction-diffusion problems (see, e.g., [25–27]). IMEX-RKC treats the moderately stiff diffusion terms explicitly and the strongly nonlinear reaction terms implicitly. The explicit treatment of the diffusion term is a key aspect in a parallel implementation since an implicit treatment needs to solve a global linear system and creates a potential bottleneck in the parallel implementation. In this work, we propose implementing the IMEX-RKC approach in a finite element space associated with a quadtree partition of the computational domain. This constitutes a novelty concerning the state-of-the-art, where such a scheme is generally adopted in a conforming discrete setting.

The paper is organized as follows. In Section 2, we present the single-phase depth-integrated mathematical model for fast landslides. Section 3 illustrates the Split IMEX-RKC TG2-PC method, first by describing the TG2-PC and the IMEX-RKC schemes we adopt and successively by dealing with the Strang split procedure. In Section 4, we analyze the reliability of the Split IMEX-RKC TG2-PC scheme through some numerical checks. In particular, after investigating the accuracy of the procedure, we show numerical evidence of the well-balancing property together with the capability to use a larger time step when compared with a basic TG2 scheme. Then, we assess the performance of the overall parallel implementation by performing a strong scalability analysis on both ideal and real satellite orography. Concluding remarks are provided in Section 5.

2. Model equations

Let us consider a rectangular computational domain, $\Omega \subset \mathbb{R}^2$, which contains a subdomain, $\Omega_w \subset \Omega$, representing the region of landslide material, varying in space and time, defined as the portion of Ω where the depth, H , of the landslide material is strictly greater than zero.

We are interested in solving the following set of nonlinear and non-conservative equations,

$$\partial_t \mathbf{q} + \nabla \cdot \mathbf{F} + \nabla \cdot \mathbf{G} + \mathbf{B} \nabla Z = \mathbf{r} \quad \text{in } \Omega_w \times (0, T], \quad (1)$$

equipped with proper boundary and initial conditions, where $\mathbf{q} = \mathbf{q}(\mathbf{x}, t) \in \mathbb{R}^4$ is the vector of conserved variables, $\mathbf{F} = \mathbf{F}(\mathbf{q}) \in \mathbb{R}^{4 \times 2}$ is the tensor of transport fluxes, $\mathbf{G} = \mathbf{G}(\mathbf{q}, \nabla \mathbf{q}) \in \mathbb{R}^{4 \times 2}$ is the tensor of diffusive fluxes, $\mathbf{B} = \mathbf{B}(\mathbf{q}) \in \mathbb{R}^{4 \times 2}$ is the matrix of the non-conservative terms, Z is the orography profile, $\mathbf{r} = \mathbf{r}(\mathbf{q}) \in \mathbb{R}^4$ is the reaction term, and $(0, T]$ denotes the time window of interest. In particular, to model the landslide run-out phase, we consider the de Saint-Venant equations (see, e.g., [28,29,5,30]), so that $\mathbf{q} = [H, U_x, U_y, Z]^T$, with U_x and U_y the mass flux associated with x - and y -direction, respectively. In more detail, the transport fluxes coincide with

$$\mathbf{F}(\mathbf{q}) = \begin{bmatrix} U_x & U_y \\ \frac{U_x^2}{H} + \frac{1}{2}gH^2 & \frac{U_y U_x}{H} \\ \frac{U_y U_x}{H} & \frac{U_y^2}{H} + \frac{1}{2}gH^2 \\ 0 & 0 \end{bmatrix}, \quad (2)$$

with g the gravitational field. The diffusive fluxes are characterized by the expressions

$$\mathbf{G}(\mathbf{q}, \nabla \mathbf{q}) = \begin{bmatrix} 0 & 0 \\ -\frac{1}{\rho}\sigma_{xx}H & -\frac{1}{\rho}\sigma_{xy}H \\ -\frac{1}{\rho}\sigma_{xy}H & -\frac{1}{\rho}\sigma_{yy}H \\ 0 & 0 \end{bmatrix}, \quad (3)$$

with ρ the material density that we assume uniform and constant, and where the set $\{\sigma_{ij}\}_{ij}$, $i, j = x, y$, defines the deviatoric part of the Cauchy stress tensor σ ; the non-conservative matrix is defined by

$$\mathbf{B}(\mathbf{q}) = \begin{bmatrix} 0 & 0 \\ gH & 0 \\ 0 & gH \\ 0 & 0 \end{bmatrix}; \quad (4)$$

the reaction term is given by

$$\mathbf{r}(\mathbf{q}) = \begin{bmatrix} 0 \\ \frac{1}{\rho} f_x^B \\ \frac{1}{\rho} f_y^B \\ 0 \end{bmatrix}, \quad (5)$$

with $f_i^B = f_i^B(\mathbf{q})$, $i = x, y$, the bed friction. In particular, we adopt the Voellmy rheology, i.e., we choose

$$f_i^B(\mathbf{q}) = - \left(p_b \tan \delta \operatorname{sgn} w_i + \rho g \frac{|w_i| w_i}{\xi} \right), \quad (6)$$

being \mathbf{w} the velocity field with components $w_i = U_i/H$, $i = x, y$ and sgn the signum function. The p_b is the basal pressure and, according to Stevino, varies linearly along the vertical axis, i.e., $p_b = p_s + \rho g H$ with p_s the atmospheric pressure, δ is the bed friction angle that we assume constant in time due to the absence of consolidation processes in the considered model, and ξ is the turbulence coefficient.

Concerning the tensor σ , following the works [31,29,32], we adopt a depth-integrated regularized visco-plastic Bingham stress model where the regularization is performed through an exponential function. Thus, we have

$$\sigma = \left(2\mu + \frac{\tau_Y(1 - e^{-N\sqrt{I_2}})}{\sqrt{I_2}} \right) \mathbf{D}, \quad (7)$$

where μ is the fluid viscosity, τ_Y is the yield shear stress, N is the regularization parameter, \mathbf{D} is the horizontal strain rate tensor defined by $\mathbf{D} = \frac{1}{2}(\nabla \mathbf{w} + \nabla \mathbf{w}^T)$, and I_2 is the second invariant of the complete depth-integrated strain tensor and is calculated following a procedure fully described in the works [5,6].

The regularization parameter N (set to 1000s in all the simulations of Section 4, as in [32]) is necessary to prevent the deviatoric stress tensor from becoming singular in the case of low strain rates, i.e., when the second invariant is close to zero. This implies that, in the limit of I_2 close to zero, the exponentially regularized rheology exists finite and is proportional to the coefficient N , that is, the apparent viscosity that multiplies the tensor \mathbf{D} in (7) becomes equal to $\bar{\mu} = 2\mu + N\tau_Y$.

Finally, we point out that the model (1) admits the steady state ‘lake-at-rest’ solution [33], i.e.,

$$\eta = H + Z = \text{constant}, \quad \mathbf{U} = [U_x, U_y]^T = \mathbf{0}, \quad (8)$$

where η is the free-surface height. In the rest of the paper, we will refer to a well-balanced numerical method when it can exactly preserve the lake-at-rest solution (see Section 4.1.2). We note that, the lake-at-rest condition leads to a balance between pressure forces and slope contributions, namely to satisfy the condition

$$\mathbf{WB} = \mathbf{0}, \quad \mathbf{WB} := \nabla \cdot \mathbf{F} + \mathbf{B} \nabla Z \quad (9)$$

in the whole domain.

3. The numerical scheme

Before considering the specific discretization we adopt, it is important to remark that model (1) is actually approximated on the whole computational spatial domain Ω rather than on the wet region Ω_w only. With this aim, we introduce a threshold H_{\min} for the depth of the landslide material, under which we assign a null velocity, thus defining the wet (dry) region as the portion of Ω where $H > H_{\min}$ ($H \leq H_{\min}$). This modeling trick considerably simplifies the numerical treatment of problem (1), since domain Ω_w varies in time and can take any possible shape; vice versa, domain Ω does coincide with a rectangle during the entire time window. This leads to the imposition of boundary conditions directly on the boundary of the computational domain, $\partial\Omega$, rather than on the wet-dry interface curve $\partial\Omega_w$ changing in time. Furthermore on the wet-dry interface

This wetting-drying method is fully conservative since drainage zones are explicitly identified. Moreover, outflow or zero mass flux boundary conditions are automatically imposed on the wet-dry interface. Thus, the mass and momentum equations reduce to

$$\begin{cases} \partial_t H = 0, \\ \mathbf{U} = \mathbf{0}, \end{cases}$$

in the dry regions, i.e. for $H \leq H_{\min}$. The wetting-drying approach is thoroughly described in [34], which is applied to the numerical solution of the semi-Lagrangian shallow water equations when resorting to a DG space discretization.

In the next two sections, we introduce the numerical schemes which are instrumental in formalizing the Split IMEX-RKC TG2-PC method proposed in this paper, see Section 3.3.

3.1. The TG2-PC scheme

The two-step Taylor-Galerkin (TG2) scheme is based on a Taylor series expansion in time which, according to [35], offers a useful alternative to a Runge-Kutta time integration when dealing with non-stiff problems. Indeed, a TG2 scheme requires performing a flux limiting procedure just once per time step, in contrast to a Runge-Kutta method which demands such a correction at each stage of the method.

In this paper, we propose a new variant to the standard explicit TG2 scheme by integrating the non-conservative contributions with a PC method. For a review of the explicit standard TG2 scheme in fast landslide simulation, we refer to [36,6].

Let us consider a hyperbolic problem with non-conservative contributions, i.e., model (1) when omitting the diffusive fluxes \mathbf{G} and the source term \mathbf{r} . This is equivalent to considering frictionless shallow-water equations in the presence of an arbitrary bottom fixed in time (i.e., with $\partial_t Z = 0$).

At a generic time t^{n+o} with $o = 0, \frac{1}{2}, 1$, after denoting by $\mathbf{Q}^{n+o} \approx \mathbf{q}^{n+o}$ the time discrete counterpart of the conservative variable at time t^{n+o} , and letting $\mathbf{F}^{n+o} = \mathbf{F}(\mathbf{Q}^{n+o})$, $\mathbf{B}^{n+o} = \mathbf{B}(\mathbf{Q}^{n+o})$, we consider the following two-step second-order semi-discrete scheme for the time-integration of system (1) between two consecutive time instants t^n and t^{n+1}

$$\begin{cases} \mathbf{Q}^{n+\frac{1}{2}} = \mathbf{Q}^n + \frac{\Delta t}{2} (-\nabla \cdot \mathbf{F}^n - \mathbf{B}^n \nabla Z^n), \\ \mathbf{Q}^{n+1} = \mathbf{Q}^n + \Delta t \left[-\nabla \cdot \mathbf{F}^{n+\frac{1}{2}} - \mathbf{B}^{n+\frac{1}{2}} \nabla Z^{n+\frac{1}{2}} \right], \end{cases} \quad (10)$$

where the first equation coincides with a first-order predictor step used to approximate the conservative variables at the intermediate time.

Now, we consider discretization in space by using the finite element method to recover the fully discrete scheme. We partition domain Ω using a family, $\{D_h\}$, of quadrilateral structured meshes with spacing h . We associate with D_h two discrete spaces, namely the space \mathbb{Q}_0 of the (discontinuous) piece-wise constant polynomials to discretize the first step in (10), and the space \mathbb{Q}_1 of the continuous piece-wise bilinear polynomials for the discretization of the second step. In particular, $\mathbf{Q}^{n+\frac{1}{2}}$ is approximated in space \mathbb{Q}_0 , while both \mathbf{Q}^n and \mathbf{Q}^{n+1} are chosen in \mathbb{Q}_1 . Spaces \mathbb{Q}_0 and \mathbb{Q}_1 are endowed with a basis, given by $\{\phi_j^{(0)}, j = 1, \dots, M\}$ and $\{\phi_i^{(1)}, i = 1, \dots, N\}$, respectively, after denoting by M the number of quadrilateral elements in D_h and by N the number of mesh nodes. Thus, the fully-discrete weak form reads

$$\begin{aligned} (\mathbf{Q}^{n+\frac{1}{2}}, \phi_j^{(0)}) &= (\mathbf{Q}^n, \phi_j^{(0)}) - \frac{\Delta t}{2} (\nabla \cdot \mathbf{F}^n, \phi_j^{(0)}) - \frac{\Delta t}{2} (\mathbf{B}^n \nabla Z^n, \phi_j^{(0)}), \\ (\mathbf{Q}^{n+1}, \phi_i^{(1)}) &= (\mathbf{Q}^n, \phi_i^{(1)}) + \Delta t (\mathbf{F}^{*,n+\frac{1}{2}}, \nabla \phi_i^{(1)}) - \Delta t (\mathbf{B}^{n+\frac{1}{2}} \nabla Z^{n+\frac{1}{2}}, \phi_i^{(1)}), \end{aligned} \quad (11)$$

for $j = 1, \dots, M$, $i = 1, \dots, N$, where (\cdot, \cdot) indicates the $L^2(\Omega)$ -scalar product, while $\mathbf{F}^{*,n+\frac{1}{2}}$ is a discretization flux that we define below. We note that, in this fully discrete weak-form, we have neglected the boundary integrals to be computed on the boundary of the computational domain $\partial\Omega$, i.e. the integral $\int_{\partial\Omega} \mathbf{F}^{*,n+\frac{1}{2}} \cdot \mathbf{n} \phi_i^{(1)} d\Omega$, where \mathbf{n} is the outward unit normal vector to the domain boundary $\partial\Omega$. It is over there that we apply boundary conditions. A complete study of boundary conditions for hyperbolic problems is beyond the study of the present work, here we consider non-reflecting boundary conditions, the reader can refer e.g. to [37] for details. Following the work [38], in the second step of the Equation (11) we rely on the mass lumping technique to avoid the inversion of the consistent mass matrix. This choice is particularly suited for a parallel implementation since each computation in the second step can be performed node-wise. Moreover, we highlight two further difficulties related to the computation of this step, i.e., the evaluation of the integral of the non-conservative product and the design of a high-order discretization flux, able to ensure both the well-balancing and the positivity-preserving property.

Let us focus on the former issue. We rely on the PC theory that provides a meaningful analytical interpretation of the non-conservative products in a weak sense [10]. Adopting a PC approach allows us to modify the scheme in order to ensure the well-balancing property by selecting an appropriate path. Even if the PC strategy has been widely applied in the literature in discrete settings like in the context of finite volume [19,39] and DG discretizations [40], to the authors' knowledge it has never been applied in a continuous finite element setting and especially in the framework of the TG2 scheme. It is worth noting that the PC method could suffer from controversial aspects. This has been widely addressed in [41], where the authors show that the PC method cannot always reproduce the solution expected by the conservative numerical solver.

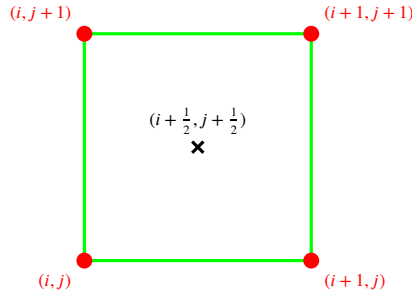


Fig. 1. Quadrilateral element centered at $(i + \frac{1}{2}, j + \frac{1}{2})$. The degrees of freedom associated with space \mathbb{Q}_1 are red-highlighted; the black cross (i.e., the barycenter of the quad) corresponds to the degree of freedom of the space \mathbb{Q}_0 .

We define a path

$$\Psi = \Psi(\mathbf{Q}_-^{n+\frac{1}{2}}, \mathbf{Q}_+^{n+\frac{1}{2}}, s) = \mathbf{Q}_-^{n+\frac{1}{2}} + s(\mathbf{Q}_+^{n+\frac{1}{2}} - \mathbf{Q}_-^{n+\frac{1}{2}}), \quad (12)$$

which connects two orography states, $\mathbf{Q}_-^{n+\frac{1}{2}}$ and $\mathbf{Q}_+^{n+\frac{1}{2}}$, related to two mesh elements sharing the same edge e , with s the parameter spanning the path, for $0 \leq s \leq 1$. We choose a standard linear path. As stated in [20], the motivation behind the specific choice of the path is the simplicity, together with the fact that the path is expected to guarantee the resulting scheme to be exactly well-balanced for the so-called lake-at-rest solutions of shallow-water type equations. Let us call \mathcal{E}_i the set of the edges e that share the node i . Then, the PC nodal formulation for the non-conservative product in the second step of (11) becomes

$$(\mathbf{B}^{n+\frac{1}{2}} \nabla Z^{n+\frac{1}{2}}, \phi_i^{(1)}) = \sum_{e \in \mathcal{E}_i} \int_0^1 \phi_i^{(1)} dl \int_0^1 \mathbf{B}(\Psi(\mathbf{Q}_-^{n+\frac{1}{2}}, \mathbf{Q}_+^{n+\frac{1}{2}}, s)) \mathbf{n}_e \partial_s \Psi ds, \quad (13)$$

where \mathbf{n}_e is the unit normal to the edge, such that $\mathbf{n}_e \cdot (\mathbf{x}_+ - \mathbf{x}_-) > 0$ with \mathbf{x}_+ and \mathbf{x}_- the coordinates of the barycenter of two elements sharing edge e , while $\partial_s \Psi$ denotes the derivative along the selected path. Finally, the two integrals are numerically computed with the trapezoidal quadrature rule.

In the following, we verify the well-balancing property of the TG2-PC scheme.

Proposition 3.1. *The fully discrete weak-form (11) with the non-conservative contribution in (13) is exact in the modeling of the lake-at-rest condition at the discrete level.*

Proof. A numerical method is well-balanced if it satisfies Equation (9) at the discrete level. To simplify the presentation, we prove that the well-balancing condition is satisfied by illustrating what happens just for the material height and the momentum equation along the x -direction. For this reason, we consider a one-dimensional motion in a two-dimensional domain.

Moreover, we make notation easier by neglecting the temporal index in the discrete variables. Thus, a discrete quantity associated with the barycenter of a quadrilateral cell refers to time $t^{n+\frac{1}{2}}$ and belongs to space \mathbb{Q}_0 . A discrete quantity associated with a node refers to time t^n and belongs to space \mathbb{Q}_1 . To make an example, $H_{i,j}$ denotes the space-time discrete counterpart of the material height, H , at the node with coordinates (i, j) and at time t^n , while one-half coordinates, such as $(i + \frac{1}{2}, j + \frac{1}{2})$, identify the degrees of freedom characterizing the space \mathbb{Q}_0 at time $t^{n+\frac{1}{2}}$. In particular, the discrete well-balancing equation at the generic coordinate (i, j) will be denoted by $\text{WB}_{(i,j)}^H$ for the material height and by $\text{WB}_{(i,j)}^{U_x}$ for the mass flux along the x -direction.

We start by considering the first step of the TG2-PC method. We take a quadrilateral element with extension $\Delta x \times \Delta y$ and we compute the one-half solution $\mathbf{Q}^{n+\frac{1}{2}}$ at the node with coordinates $(i + \frac{1}{2}, j + \frac{1}{2})$ (see Fig. 1).

We denote by $H^{n,2}$ the square of the space-time discrete material height at time t^n , and we select it in \mathbb{Q}_1 . By integrating exactly the balancing integrals in the first step of the TG2-PC method, we obtain the following well-balancing condition for the mass flux U_x at the node $(i + \frac{1}{2}, j + \frac{1}{2})$,

$$\begin{aligned} \text{WB}_{i+\frac{1}{2},j+\frac{1}{2}}^{U_x} &= \left(\frac{1}{2} g \partial_x H^{n,2}, \phi_{i+\frac{1}{2},j+\frac{1}{2}}^{(0)} \right) + \left(g H^n \partial_x Z^n, \phi_{i+\frac{1}{2},j+\frac{1}{2}}^{(0)} \right) \\ &= \left(g H^n \partial_x H^n, \phi_{i+\frac{1}{2},j+\frac{1}{2}}^{(0)} \right) + \left(g H^n \partial_x Z^n, \phi_{i+\frac{1}{2},j+\frac{1}{2}}^{(0)} \right) \\ &= \left(g H^n \partial_x (H^n + Z^n), \phi_{i+\frac{1}{2},j+\frac{1}{2}}^{(0)} \right) = 0. \end{aligned} \quad (14)$$

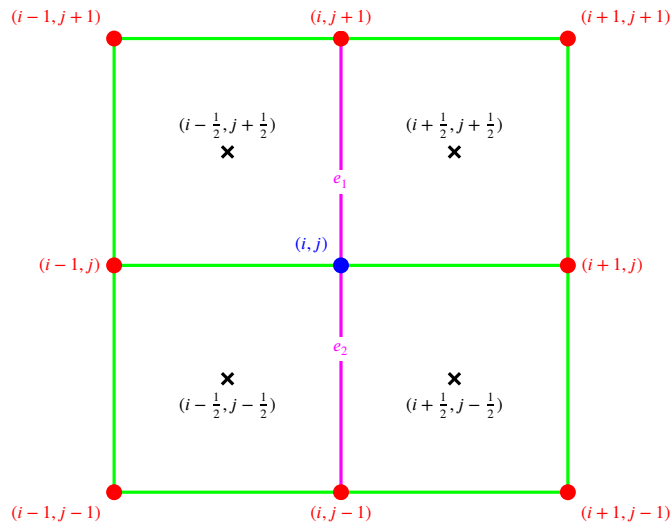


Fig. 2. Elements sharing node (i, j) (in blue). The other degrees of freedom associated with space \mathbb{Q}_1 are red-highlighted; the degrees of freedom of space \mathbb{Q}_0 are depicted with the black cross. Two edges e_1, e_2 are highlighted in magenta needed for the PC method.

This chain of equalities is obtained by exploiting the hypothesis of null mass flux $U_x^n = 0$ at time t^n , together with the relation $H^n + Z^n = \text{constant}$. These hypotheses are true since the generic time t^n does initially coincide with the initial condition. We can conclude that the first step of the TG2-PC scheme is exactly well-balanced. Indeed, considering again $U_x^n = 0$, one obtains $\text{WB}_{i+\frac{1}{2}, j+\frac{1}{2}}^H = (\partial_x U_x^n, \phi_{i+\frac{1}{2}, j+\frac{1}{2}}^{(0)}) = 0$. Moreover, we have exploited the fact that we can compute the spatial partial derivative in the element with cell center $(i + \frac{1}{2}, j + \frac{1}{2})$ since functions in \mathbb{Q}_1 are linear in the spatial coordinates. In this way, the first step of the TG2-PC method does not add any particular complication and serves just as an input to the second step, according to a predictor/corrector paradigm [22, 21].

We now check whether the well-balancing property is satisfied in the second step of the TG2-PC scheme. To this aim, we consider the four elements with extension $\Delta x \times \Delta y$ sharing the generic internal node (i, j) (see Fig. 2), where internal means that it is not a boundary node (i.e., it does not belong to $\partial\Omega$). We compute the value of the updated solution \mathbf{Q}^{n+1} at node (i, j) . In particular, in the figure, we identify in magenta the edges where we compute the PC integral. We observe that, for the computation of the PC integral, we consider just the edges having normal aligned with the x -direction. Indeed, while expression (13) is fully general, here we particularize such an expression to the U_x -component of the vector WB defined in (9). This means that, when computing the product between \mathbf{B} and \mathbf{n}_e in (13), only the second row of \mathbf{B} is involved, i.e., only the edges with the normal aligned to the x -axis provide a non-null contribution to the computation of the following quantity $\text{WB}_{i,j}^{U_x}$.

Denoting by $H^{n+\frac{1}{2},2}$ the square of the space-time discrete quantity $H^{n+\frac{1}{2}}$ belonging to \mathbb{Q}_0 and at time $t^{n+\frac{1}{2}}$, after integrating exactly the conservative flux and by using the trapezoidal rule to integrate the PC formulation for the continuous space \mathbb{Q}_1 , we obtain the following well-balancing property at the discrete level,

$$\begin{aligned} \text{WB}_{i,j}^{U_x} &= \left(\frac{1}{2} g H^{n+\frac{1}{2},2}, \partial_x \phi_{i,j}^{(1)} \right) - \left(g H^{n+\frac{1}{2}} \partial_x Z^{n+\frac{1}{2}}, \phi_{i,j}^{(1)} \right) \\ &= \int_0^{\Delta x} \int_0^{\Delta y} \frac{1}{\Delta x} \frac{y}{\Delta y} \frac{1}{2} g H_{i-\frac{1}{2},j-\frac{1}{2}}^2 dx dy \\ &\quad + \int_0^{\Delta x} \int_0^{\Delta y} \frac{-1}{\Delta x} \frac{y}{\Delta y} \frac{1}{2} g H_{i+\frac{1}{2},j-\frac{1}{2}}^2 dx dy \\ &\quad + \int_0^{\Delta x} \int_0^{\Delta y} \frac{1}{\Delta x} \left(1 - \frac{y}{\Delta y} \right) \frac{1}{2} g H_{i-\frac{1}{2},j+\frac{1}{2}}^2 dx dy \\ &\quad + \int_0^{\Delta x} \int_0^{\Delta y} \frac{-1}{\Delta x} \left(1 - \frac{y}{\Delta y} \right) \frac{1}{2} g H_{i+\frac{1}{2},j+\frac{1}{2}}^2 dx dy \end{aligned}$$

$$\begin{aligned}
& - \sum_{k=1,2} \int_{e_k} \phi_{i,j}^{(1)} dy \int_0^1 g \Psi_H(\mathbf{Q}_{-}^{n+\frac{1}{2}}, \mathbf{Q}_{+}^{n+\frac{1}{2}}, s) \partial_s \Psi_Z ds \\
& = \frac{\Delta y}{2} \left(\frac{1}{2} g H_{i-\frac{1}{2}, j+\frac{1}{2}}^2 + \frac{1}{2} g H_{i-\frac{1}{2}, j-\frac{1}{2}}^2 \right) \\
& - \frac{\Delta y}{2} \left(\frac{1}{2} g H_{i+\frac{1}{2}, j+\frac{1}{2}}^2 + \frac{1}{2} g H_{i+\frac{1}{2}, j-\frac{1}{2}}^2 \right) \\
& - \frac{\Delta y}{2} \frac{1}{2} g \left(H_{i-\frac{1}{2}, j+\frac{1}{2}} + H_{i+\frac{1}{2}, j+\frac{1}{2}} \right) \left(Z_{i+\frac{1}{2}, j+\frac{1}{2}} - Z_{i-\frac{1}{2}, j+\frac{1}{2}} \right) \\
& - \frac{\Delta y}{2} \frac{1}{2} g \left(H_{i-\frac{1}{2}, j-\frac{1}{2}} + H_{i+\frac{1}{2}, j-\frac{1}{2}} \right) \left(Z_{i+\frac{1}{2}, j-\frac{1}{2}} - Z_{i-\frac{1}{2}, j-\frac{1}{2}} \right) \\
& = \frac{1}{2} g \frac{\Delta y}{2} \left(H_{i-\frac{1}{2}, j-\frac{1}{2}} + H_{i-\frac{1}{2}, j+\frac{1}{2}} \right) \left(H_{i-\frac{1}{2}, j-\frac{1}{2}} + Z_{i-\frac{1}{2}, j-\frac{1}{2}} \right) \\
& - \frac{1}{2} g \frac{\Delta y}{2} \left(H_{i-\frac{1}{2}, j-\frac{1}{2}} + H_{i-\frac{1}{2}, j+\frac{1}{2}} \right) \left(H_{i-\frac{1}{2}, j+\frac{1}{2}} + Z_{i-\frac{1}{2}, j+\frac{1}{2}} \right) \\
& + \frac{1}{2} g \frac{\Delta y}{2} \left(H_{i+\frac{1}{2}, j-\frac{1}{2}} + H_{i+\frac{1}{2}, j+\frac{1}{2}} \right) \left(H_{i+\frac{1}{2}, j-\frac{1}{2}} + Z_{i+\frac{1}{2}, j-\frac{1}{2}} \right) \\
& - \frac{1}{2} g \frac{\Delta y}{2} \left(H_{i+\frac{1}{2}, j-\frac{1}{2}} + H_{i+\frac{1}{2}, j+\frac{1}{2}} \right) \left(H_{i+\frac{1}{2}, j+\frac{1}{2}} + Z_{i+\frac{1}{2}, j+\frac{1}{2}} \right) = 0,
\end{aligned} \tag{15}$$

where $\Psi_H(\mathbf{Q}_{-}^{n+\frac{1}{2}}, \mathbf{Q}_{+}^{n+\frac{1}{2}}, s)$, $\Psi_Z(\mathbf{Q}_{-}^{n+\frac{1}{2}}, \mathbf{Q}_{+}^{n+\frac{1}{2}}, s)$ denote the H and Z components of the path Ψ . We note that $\text{WB}_{i,j}^{U_x}$ is zero at the discrete level, being the first step of the TG2-PC scheme well-balanced. Indeed, since the well-balancing condition is satisfied in the first step, we have $H_{i,\bar{j}} + Z_{i,\bar{j}} = \text{constant}$ for $\bar{i} = i - \frac{1}{2}, i + \frac{1}{2}$ and $\bar{j} = j - \frac{1}{2}, j + \frac{1}{2}$ that causes $\text{WB}_{i,j}^{U_x}$ to be zero. In addition, since we do not have any non-conservative products in the mass equation, we trivially get $\text{WB}_{i,j}^H = (U_x^{n+\frac{1}{2}}, \partial_x \phi_{i,j}^{(1)}) = 0$, which is satisfied thanks to the well-balancing property of the first step. This is sufficient to prove that the well-balancing condition is also satisfied at the second step of the TG2-PC method. To obtain expression (15), we have assumed a null momentum flux at time $t^{n+\frac{1}{2}}$, being the first step of the numerical scheme exactly well-balanced; moreover, we have used the algebraic relation $a^2 - b^2 = (a+b)(a-b)$, with $a, b \in \mathbb{R}$. \square

We remark that we have omitted the Rusanov flux contribution in the proof of Proposition 3.1. In general, this term might deteriorate the well-balancing property of the PC method. Thus, particular care is needed to design a diffusive flux capable of preserving this condition (we refer to the end of Section 3.1 for more details).

We now address the design of a high-order discretization flux $\mathbf{F}^{*,n+\frac{1}{2}}$. The TG2 scheme is neither monotone nor positivity-preserving, being second-order space-time accurate [42]. Here, we adopt Zalesak's multidimensional Flux Corrected Transport (FCT) (see [43–45] for more details), in order to prevent the rise of spurious oscillations near discontinuities, i.e., the Gibbs phenomenon, so to maintain an oscillation-free positivity-preserving physical solution. As already underlined in the work [6], to this aim, we adopt the Rusanov first-order monotone discretization flux weighted by the correction flux-limiting coefficient. However, we remark that the FCT strategy does not preserve the well-balanced property of the numerical scheme. This is a common feature of flux limiters, which has already been addressed in the case of a DG discretization [46]. Below, we adopt a procedure similar to the one used in this work for approximating shallow water equations with a DG approach.

To formalize the adopted well-balanced FCT method, let us consider a single quadrilateral element, Q , of the domain discretization with resolution $\Delta x \times \Delta y$ and consider the variable $\mathbf{v} = \mathbf{U}\mathbf{q}$, with

$$\mathbf{U} = \begin{bmatrix} 1 & 0 & 0 & u \\ 0 & 1 & 0 & 0 \\ 0 & 0 & 1 & 0 \\ 0 & 0 & 0 & 0 \end{bmatrix} \tag{16}$$

and $u = u(H - H_{\min})$ the Heaviside step function. Then, the Rusanov anti-diffusive flux is defined as,

$$\delta \mathbf{F}_Q^n = \left(\min \left(\frac{\Delta x}{\Delta t}, \frac{\Delta y}{\Delta t} \right) \right) \frac{1}{2\Delta t} (\nabla \mathbf{V}^n, \phi_Q^{(0)}), \tag{17}$$

with $\phi_Q^{(0)}$ the \mathbb{Q}_0 -basis function associated with element Q and \mathbf{V}^n the time discrete counter-part of the variable \mathbf{v} , i.e., $\mathbf{V}^n = \mathbf{U}^n \mathbf{Q}^n$. The exact integration in (17) results in an anti-diffusive flux, coinciding with a linear function of the ratios $\frac{\Delta x}{\Delta t}$ and $\frac{\Delta y}{\Delta t}$. Thanks to the Courant–Friedrichs–Lewy (CFL) condition, these ratios are lower bounded by the maximum simple wave speed modulus in Q ,

along the x - and y -direction. The simple waves correspond to the eigenvalues of the full semi-linear system, namely the system that contains both conservative and non-conservative contributions. Finally, the discrete flux in the element Q is given by

$$\mathbf{F}_Q^{*,n+\frac{1}{2}} = (\mathbf{F}_Q^{n+\frac{1}{2}} - \delta \mathbf{F}_Q^n) + \alpha_Q \delta \mathbf{F}_Q^n, \quad (18)$$

where $\alpha_Q \in \mathbb{Q}_0$ denotes the piece-wise constant FCT coefficient defined according to the well-known Zalesak procedure [43–45] (for the specific implementation, we refer to [6]). Considering that the Zalesak procedure provides a positivity-preserving approximation only if the low order scheme is positivity-preserving. In particular, for the low-order discretization flux we are considering, the following result holds,

Proposition 3.2. *The low-order TG2-PC scheme yields a positivity-preserving discretization for the free-surface height.*

Proof. To consider the low order scheme, we set $\mathbf{F}_Q^{*,n+\frac{1}{2}} = \mathbf{F}_Q^{n+\frac{1}{2}} - \delta \mathbf{F}_Q^n$ (i.e., $\alpha_Q = 0$) in (18). In addition, to ease the presentation, we refer to a one-dimensional motion, i.e., we set $U_y = 0$, while adopting the same notation as in Proposition 3.1, and particularly refer to Fig. 2. Furthermore, due to the one-dimensional motion assumption, we will avoid any dependency on the index j , i.e., associated to the y -coordinate.

We first focus on the case where the topography describes a flat bottom, namely $Z(\mathbf{x}) = 0$. In such a case, the TG2 scheme (i.e., $\delta \mathbf{F}_Q^n = 0$), when applied to the frictionless shallow water equations, reads

$$\begin{aligned} H_{i,j}^{n+1} &= H_{i,j}^n + \frac{\Delta t}{\Delta x} (U_{x,i-\frac{1}{2},j-\frac{1}{2}}^{n+\frac{1}{2}} - U_{x,i+\frac{1}{2},j-\frac{1}{2}}^{n+\frac{1}{2}}), \\ U_{x,i-\frac{1}{2},j-\frac{1}{2}}^{n+\frac{1}{2}} &= \frac{U_{x,i,j}^n + U_{x,i-1,j}^n}{2} + \frac{\Delta t}{2\Delta x} (F_{i-1,j}^n - F_{i,j}^n), \\ U_{x,i+\frac{1}{2},j-\frac{1}{2}}^{n+\frac{1}{2}} &= \frac{U_{x,i,j}^n + U_{x,i+1,j}^n}{2} + \frac{\Delta t}{2\Delta x} (F_{i,j}^n - F_{i+1,j}^n), \end{aligned}$$

where $F = H w_x^2 + \frac{1}{2} g H^2$. Then, the material height update is provided by

$$\begin{aligned} H_{i,j}^{n+1} &= H_{i,j}^n (1 - w_{x,i,j}^{2,n} \bar{v}^2 - g H_{i,j}^n \frac{\bar{v}^2}{2}) \\ &\quad + H_{i-1,j}^n (w_{x,i-1,j}^{2,n} \frac{\bar{v}^2}{2} + g H_{i-1,j}^n \frac{\bar{v}^2}{4} + w_{x,i-1,j}^n \frac{\bar{v}}{2}) \\ &\quad + H_{i+1,j}^n (w_{x,i+1,j}^{2,n} \frac{\bar{v}^2}{2} + g H_{i+1,j}^n \frac{\bar{v}^2}{4} - w_{x,i+1,j}^n \frac{\bar{v}}{2}), \end{aligned} \quad (19)$$

where quantity $\bar{v} = \frac{\Delta t}{\Delta x}$ is linked to the nodal CFL number ν through the relation $\nu = \bar{v} \lambda$, with $\lambda = |w_x| + c$ the maximum eigenvalue in modulus, with $c = \sqrt{gH}$ the celerity. Notice that the dependence of both ν and λ on the nodal indices is neglected for simplicity. Analogously, we omit any temporal superscript and spatial subscript to ease the presentation.

From (19), it follows that the TG2 method is not positivity-preserving. Indeed, by algebraically manipulating the coefficients multiplying $H_{i\pm 1,j}^n$ in the two last lines of (19), we have to ensure that

$$\nu \geq \pm \frac{w_x \lambda}{w_x^2 + c^2/2},$$

i.e. that

$$\nu \geq \frac{|w_x| \lambda}{w_x^2 + c^2/2}$$

in order to guarantee the positivity of the updated material height. It follows that, the right hand side is greater than one for Froude numbers $Fr = \frac{|w_x|}{c}$ greater than $\frac{1}{2}$, which proves that the TG2 method does not preserve the positivity-preserving property for all the flow conditions.

However, if we add the extra numerical diffusion given by the Rusanov flux in (17) (i.e., $\delta \mathbf{F}_Q^n \neq 0$), i.e.,

$$\begin{aligned} H_{i,j}^{n+1} &= H_{i,j}^n (1 - w_{x,i,j}^{2,n} \bar{v}^2 - g H_{i,j}^n \frac{\bar{v}^2}{2} - \nu) \\ &\quad + H_{i-1,j}^n (w_{x,i-1,j}^{2,n} \frac{\bar{v}^2}{2} + g H_{i-1,j}^n \frac{\bar{v}^2}{4} + w_{x,i-1,j}^n \frac{\bar{v}}{2} + \frac{\nu}{2}) \\ &\quad + H_{i+1,j}^n (w_{x,i+1,j}^{2,n} \frac{\bar{v}^2}{2} + g H_{i+1,j}^n \frac{\bar{v}^2}{4} - w_{x,i+1,j}^n \frac{\bar{v}}{2} + \frac{\nu}{2}), \end{aligned} \quad (20)$$

then, the low-order solution now is positivity-preserving if conditions

$$\begin{cases} 1 - w_x^2 \bar{v}^2 - c^2 \frac{\bar{v}^2}{2} - v & \geq 0, \\ w_x^2 \frac{\bar{v}^2}{2} + c^2 \frac{\bar{v}^2}{4} \pm w_x \frac{\bar{v}}{2} + \frac{v}{2} & \geq 0 \end{cases} \quad (21)$$

are satisfied. After simple algebra, we can simplify the second equation in (21) to

$$v \geq \frac{-1 \pm \frac{w_x}{\lambda}}{w_x^2 + \frac{c^2}{2}} \lambda^2,$$

which results in the following conditions to be satisfied

$$v \geq \frac{|w_x| - \lambda}{w_x^2 + \frac{c^2}{2}} \lambda = \frac{-c\lambda}{w_x^2 + \frac{c^2}{2}}. \quad (22)$$

It turns out that equation (22) is always satisfied since c is positive by definition. Concerning the first inequality in (21), it follows that

$$1 - v^2 - v \geq 0, \quad (23)$$

is a sufficient condition to guarantee positivity-preserving since $v^2 > \bar{v}^2(w_x^2 + c^2/2)$ holds in every flow regime. Thus, the CFL number is expected to satisfy the two-side inequality

$$\frac{-1 - \sqrt{5}}{2} \leq v \leq \frac{-1 + \sqrt{5}}{2}.$$

We observe that while the left constraint is always satisfied, the condition on the right-hand side leads to an actual bound on the CFL number, namely on the positivity-preserving property for a low-order TG2 scheme. In particular, the FCT strategy ensures a global positivity-preserving scheme, with a second-order accurate solution.

In the more general case of a non-flat orography ($Z(\mathbf{x}) \neq 0$), the positivity-preserving feature can be proved on the nodal free-surface height, $\eta_{i,j}^{n+1}$. Since $\partial_t Z = 0$, it suffices to modify equation (19) by adding the quantity $Z_{i,j}^n$.

This leads to an equation for the variable $\eta_{i,j}^{n+1}$ consisting of two terms, the former equal to the contribution associated with the case $Z(\mathbf{x}) = 0$, the latter given by

$$\frac{\bar{v}^2}{2} (Z_{i-1,j}^n \bar{c}_l^2 - Z_{i,j}^n (\bar{c}_l^2 + \bar{c}_r^2) + Z_{i+1,j}^n \bar{c}_r^2), \quad (24)$$

with $\bar{c}_l^2 = \frac{g(H_{i,j}^n + H_{i-1,j}^n)}{2}$, $\bar{c}_r^2 = \frac{g(H_{i+1,j}^n + H_{i,j}^n)}{2}$. The new contribution in (24) modifies the two constraints in (21), when investigating the positivity-preserving condition. In particular, after exploiting definition (17), inequality $v^2 > \frac{\bar{v}^2}{2} \bar{c}^2$, and properly collecting the η - and the Z -contributions, we are led to control the coefficient multiplying $Z_{i,j}^n$, i.e., to impose

$$1 - v^2 - v \geq 0,$$

exactly as in (23). The positivity-preserving property is thus proved in terms of the free-surface variable η . \square

3.2. The second order IMEX-RKC finite element scheme

To face the stiffness of the diffusion and source terms, we resort to a second-order space-time Implicit–Explicit Runge–Kutta–Chebyshev (IMEX-RKC) finite element scheme. This method avoids building a global matrix, as in the case of implicit schemes, while maintaining the node-wise operation structure suited to a parallel implementation.

With this aim, we start from a diffusion-reaction equation, i.e., we neglect the hyperbolic contribution in model (1) coinciding with the terms depending on \mathbf{F} and \mathbf{B} . We consider the corresponding spatial discretization based on the finite element space \mathbb{Q}_1 associated with the quadrilateral structured partition \mathcal{D}_h of Ω . Thus, at each node i , for $i = 1, \dots, N$, we deal with the semi-discrete problem

$$\begin{cases} \frac{d}{dt} \mathbf{V}_i = \mathbf{F}_D(t, \mathbf{V}_{\mathcal{N}_i}) + \mathbf{F}_R(t, \mathbf{V}_i), \\ \mathbf{F}_D(t, \mathbf{V}_{\mathcal{N}_i}) = (\mathbf{G}, \nabla \phi_i^{(1)}), \\ \mathbf{F}_R(t, \mathbf{V}_i) = (\mathbf{r}, \phi_i^{(1)}), \end{cases} \quad (25)$$

where $\mathbf{V}_i = (\mathbf{q}, \phi_i^{(1)})$ is a vector of functions in time, which discretizes the conserved variable \mathbf{q} at the node i , the integral being computed with a mass lumping approach. Accordingly, $\mathbf{F}_D(t, \mathbf{V}_{\mathcal{N}_i})$ and $\mathbf{F}_R(t, \mathbf{V}_i)$ provide the spatial discretization of the diffusive

fluxes and of the reaction term, respectively, symbol $\mathbf{V}_{\mathcal{N}_i}$ denoting the discretization of \mathbf{q} at the nodes in the patch of elements associated with node i .

Finally, we note that, in this semi-discrete formulation, we have omitted the boundary conditions on the diffusive flux, we have set $\int_{\partial\Omega} \mathbf{G} \mathbf{n} \phi_i^{(1)} d\mathbf{\Sigma} = \mathbf{0}$. Again, a complete treatment of boundary conditions, in this case for purely diffusive problems, is beyond the scope of the present work. We consider null boundary fluxes for simplicity and also that most of the influence is due to the transport fluxes in an advection-dominated problem.

It is well-known that a spatial discretization through linear finite elements of the diffusive fluxes leads to a space-discrete operator whose eigenvalues lie on the real axis and are all negatives, refer to [24,47]. To this aim we consider the IMEX-RKC time integration scheme [23]. Which is an extension of the RKC scheme designed for the time integration of diffusion problems [24] and that has already been applied in the framework of linear finite elements in the work [27]. The second-order IMEX-RKC scheme can be formalized in such a way: given the numerical solution \mathbf{V}_i^n at time t^n , the updated solution, \mathbf{V}_i^{n+1} , is computed by:

$$\left\{ \begin{array}{l} \mathbf{W}_i^0 = \mathbf{V}_i^n, \\ \mathbf{W}_i^1 - \tilde{\mu}_1 \Delta t \mathbf{F}_R^1(\mathbf{W}_i^1) = \mathbf{W}_i^0 + \tilde{\mu}_1 \Delta t \mathbf{F}_D^0(\mathbf{W}_{\mathcal{N}_i}^0), \\ \mathbf{W}_i^j - \tilde{\mu}_1 \Delta t \mathbf{F}_R^j(\mathbf{W}_i^j) = (1 - \mu_j - \nu_j) \mathbf{W}_i^0 + \mu_j \mathbf{W}_i^{j-1} + \nu_j \mathbf{W}_i^{j-2} \\ \quad + \tilde{\mu}_j \Delta t \mathbf{F}_D^{j-1}(\mathbf{W}_{\mathcal{N}_i}^{j-1}) + \tilde{\gamma}_j \Delta t \mathbf{F}_D^0(\mathbf{W}_{\mathcal{N}_i}^0) \\ \quad + (\tilde{\gamma}_j \tilde{\mu}_1 \mu_j / \tilde{\mu}_j - (1 - \mu_j - \nu_j) \tilde{\mu}_1) \Delta t \mathbf{F}_R^0(\mathbf{W}_i^0) \\ \quad - \nu_j \tilde{\mu}_1 \Delta t \mathbf{F}_R^{j-2}(\mathbf{W}_i^{j-2}), \quad j = 2, \dots, m, \\ \mathbf{V}_i^{n+1} = \mathbf{W}_i^m, \end{array} \right. \quad (26)$$

where $\mathbf{W}_i^0, \dots, \mathbf{W}_i^m$ are intermediate vectors in the node i , fluxes $\mathbf{F}_D^j(\mathbf{W}_{\mathcal{N}_i}^j)$, $\mathbf{F}_R^j(\mathbf{W}_i^j)$ stand for $\mathbf{F}_D(t^n + c_j \Delta t, \mathbf{W}_{\mathcal{N}_i}^j)$, $\mathbf{F}_R(t^n + c_j \Delta t, \mathbf{W}_i^j)$ respectively, with $0 = c_0 < c_1 < \dots < c_m = 1$. Again, $\mathbf{W}_{\mathcal{N}_i}^j$ refers to the set of vectors \mathbf{W}_k^j , $k = 1, \dots, N$ defined on the set of nodes belonging to the set of elements sharing the node i with the node i itself. The number m of stages required to stabilize the second-order RKC method depends on the stiffness of the diffusion term. As derived in [23], we set

$$m = 1 + \left\lceil \left(1 + \frac{\Delta t \sigma_J}{0.653} \right)^{\frac{1}{2}} \right\rceil, \quad (27)$$

with σ_J the spectral radius of the Jacobian matrix associated with the space-discrete diffusion operator \mathbf{F}_D . In particular, we estimate σ_J with the Gershgorin circle theorem while we compute the derivatives involved in the definition of the Jacobian matrix by resorting to numerical differentiation. Note that, in applications where the diffusion term is very stiff, the spectral radius may become very large and, consequently, the RKC scheme few effective in practice since requiring a significant number of internal stages to stabilize. Vice versa, formula (27) preserves a meaning in the case of a mildly stiff diffusion operator and severely stiff reaction terms, as for the problem we are dealing with in this paper.

Concerning the several coefficients involved in (26), we adopt the definitions provided in [23], that we supply here for completeness. With this aim, we introduce the Chebyshev polynomials of the first kind, defined by the recursive relation

$$T_0(x) = 1, \quad T_1(x) = x, \quad T_j(x) = 2xT_{j-1}(x) - T_{j-2}(x), \quad (28)$$

for $2 \leq j \leq m$ and $x \in \mathbb{R}$, where index j keeps trace of the polynomial degree; the positive real parameter ϵ , known as dumping parameter, that we set to $2/13$ in order to ensure a second order scheme as underlined in [24,23]; quantities

$$\omega_0 = 1 + \frac{\epsilon}{m^2}, \quad \omega_1 = \frac{T'_m(\omega_0)}{T''_m(\omega_0)}; \quad b_0 = b_1 = b_2, \quad b_j = \frac{T''_j(\omega_0)}{[T'_j(\omega_0)]^2}.$$

Thus, coefficients $\mu_j, \nu_j, \tilde{\mu}_j, \tilde{\gamma}_j$ and c_j are computed by

$$\mu_j = \frac{2b_j\omega_0}{b_{j-1}}, \quad \nu_j = \frac{-b_j}{b_{j-2}}, \quad \tilde{\mu}_j = \frac{2b_j\omega_1}{b_{j-1}} \quad \text{with} \quad \tilde{\mu}_1 = b_1\omega_1, \\ \tilde{\gamma}_j = -(1 - b_{j-1}T_{j-1}(\omega_0))\tilde{\mu}_j, \quad c_j = \frac{T'_m(\omega_0)}{T''_m(\omega_0)} \frac{T''_j(\omega_0)}{T'_j(\omega_0)} \quad \text{with} \quad c_0 = 0, \quad c_1 = \frac{c_2}{4\omega_0},$$

with $2 \leq j \leq m$.

We observe that the explicit treatment of the diffusion term in (26) leads to a nonlinear algebraic system of equations that is not coupled in space. Thus, a single nonlinear equation has to be solved at each mesh node and at each internal stage of the IMEX-RKC method. This represents a key aspect in a parallel implementation since leading to a fully decoupled system as for the TG2 scheme. Since the mass conservation equation is independent of the diffusion term, the RKC internal stages are performed just for the momentum equation. Furthermore, the bed friction term included in \mathbf{F}_R depends on the x - and y -mass fluxes separately (see

the rheology law in (6)), so that the non-linearity on each mesh node can be tackled with a scalar semi-smooth Newton method along both the x - and y -direction without requiring a matrix inversion. The semi-smooth Newton method adopted is similar to the one described in [48–50] in the context of contact problems. The choice for a semi-smooth scheme is because the bed friction is a function of the absolute value of the velocity components, thus resulting in a piece-wise differentiable function and to the presence of a signum function. In particular, we consider a linear relaxation of the signum function in (6) to ensure piece-wise differentiability. Thus, for $x \in \mathbb{R}$, we replace $\text{sgn}(x)$ with the linear relaxation

$$\text{sgn}_\gamma(x) = \begin{cases} 1 & \text{if } x > \gamma, \\ -1 & \text{if } x < -\gamma, \\ \frac{x}{\gamma} & \text{otherwise,} \end{cases} \quad (29)$$

such that $\text{sgn}(x) = \lim_{\gamma \rightarrow 0} \text{sgn}_\gamma(x)$, with γ a strictly positive relaxation parameter set to 10^{-2} in the simulation we present here.

The selected time discretization in the presence of a \mathbb{Q}_1 spatial finite element discretization leads to a numerical scheme which is second order in space and time.

3.3. Strang splitting IMEX-RKC TG2-PC method

In this section, we establish the approximation scheme we adopt for the numerical assessment in the next section. The basic remark is that in model (1) the transport and the diffusion-reaction contributions exhibit completely different characteristics from a numerical point of view. This justifies adopting a splitting method [8,7] to achieve an efficient integration in time so that each term can be integrated using the most suitable scheme. In this work, we resort to the Strang splitting, which is second-order accurate and strongly stable [8].

To simplify the presentation, we define the transport and the diffusion-reaction continuous operators as $\mathcal{T}(\mathbf{q}) = -\nabla \cdot \mathbf{F} - \mathbf{B}\nabla Z$ and $D(\mathbf{q}, \nabla \mathbf{q}) = \mathbf{r} - \nabla \cdot \mathbf{G}$, respectively. The Strang splitting method coincides with the following three-step procedure: given \mathbf{q}^n ,

$$\begin{aligned} \partial_t \mathbf{q}^{(1)} &= \mathcal{T}(\mathbf{q}^{(1)}) \quad \text{with} \quad \mathbf{q}^{(1)}(\mathbf{x}, t^n) = \mathbf{q}^n, \\ \partial_t \mathbf{q}^{(2)} &= D(\mathbf{q}^{(2)}, \nabla \mathbf{q}^{(2)}) \quad \text{with} \quad \mathbf{q}^{(2)}(\mathbf{x}, t^n) = \mathbf{q}^{(1)}\left(\mathbf{x}, t^n + \frac{\Delta t}{2}\right), \\ \partial_t \mathbf{q}^{(3)} &= \mathcal{T}(\mathbf{q}^{(3)}) \quad \text{with} \quad \mathbf{q}^{(3)}\left(\mathbf{x}, t^n + \frac{\Delta t}{2}\right) = \mathbf{q}^{(2)}(\mathbf{x}, t^n + \Delta t), \\ \mathbf{q}^{n+1} &= \mathbf{q}^{(3)}(\mathbf{x}, t^n + \Delta t), \end{aligned}$$

for $n \geq 0$. Then, we integrate the first and third steps with the TG2-PC method, while we use the IMEX-RKC finite element scheme to integrate the second step, which involves the stiff reaction-diffusion operator. Hereafter we call this scheme as Split IMEX-RKC TG2-PC method.

Note that, for stability reasons, the complete scheme is only subject to the CFL condition of the transport operator. Indeed, the IMEX-RKC finite element scheme is unconditionally stable and thus does not require any time step restriction for stability. To this aim, we compute the time step restriction based on the time step Δt . It is clear that, for stability reasons, the CFL condition can be maximum equal to 2 considering that the first and third steps of the Strang splitting procedure advance with a time step equal to $\frac{\Delta t}{2}$. This constitutes a key difference compared to the TG2 method [36,5,4,6], where a more restrictive time step is usually necessary to cope with the stiffness of the reaction term as well as to satisfy the time step restriction induced by the diffusion term that scales as h^{-2} .

4. Numerical results

We present the results of some simulations performed to assess the performance of the numerical scheme presented in the previous section. We will also compare the proposed scheme with a standard explicit TG2 method in terms of computational efficiency in the context of fast landslides modeling [36,5,4,6]. In more detail, in Section 4.1, we discuss the reliability of the Split IMEX-RKC TG2-PC method by investigating the accuracy and the well-balancing of the numerical scheme. The implementation efficiency is analyzed in Section 4.2, where we present three idealized tests with increasing complexity. Finally, in Section 4.3, we consider a real case study by resorting to a space wet-dry interface tracking mesh adaptation procedure.

The numerical framework has been implemented using the parallel library, *bim++* [51,52,6], written in C++, which implements partial differential operator discretization, recovery-based error estimators and metric-based mesh adaptation procedures on hierarchical quadtree meshes. In particular, in *bim++* mesh refinement, coarsening, balancing, and partitioning use functionalities offered by the library *p4est* [53]. For more details about the adopted space adaptation procedure, the reader can refer to [51,6]. Concerning the time discretization, we vary the time step based on the CFL condition by setting, if not otherwise stated, the CFL value to 0.9 so that the positivity-preserving constraint on the free-surface is guaranteed at the first and third Strang splitting steps. In addition, in Section 4.2.1 we show the results of the proposed discretization method when considering a CFL number considerably greater than one.

We define by L_x and L_y respectively the x - and y -extensions of the computational domain Ω .

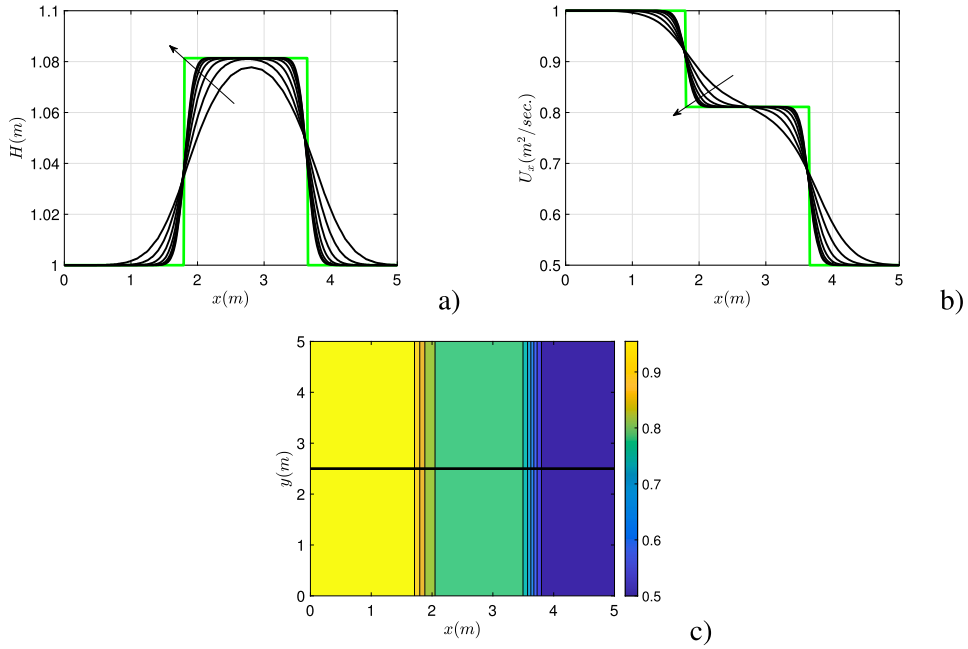


Fig. 3. Accuracy tests. Viscous dam-break problem. Panels a), b): comparison between the analytical inviscid solution (in green) and the Split IMEX-RKC TG2-PC viscous solution (in black), for various levels of mesh refinement (the arrows highlight the increasing values of l); Panel c): isolines of H , with black-highlighted the line $y = L_y/2$ along which we compute the one-dimensional solution shown in panels a), b).

From a computational viewpoint, we set the threshold, $H_{\min} = 10^{-5} m$, on the material height, such that under this threshold we have a null velocity. Finally, as mentioned in Section 3.2, we numerically compute the spectral radius, σ_J , of the Jacobian matrix of the space-discrete diffusive fluxes needed to provide an estimation of the number of stages required by the RKC scheme (equation (27)). Since the resulting space-discrete diffusion operator is a function of just the momentum fluxes, we consider an increment on U_x and U_y , set to 10^{-8} for both the components, in the context of the numerical computation of the Jacobian matrix. We perform all the calculations in double precision.

We run the simulations presented in Sections 4.2.2, 4.2.3, 4.3 on the same supercomputer architecture used in [6], the CINE-CA GALILEO100. In particular, we perform the compilation and linking steps with gcc-10 and OpenMPI 4.1.1. For all the other experiments, we use a laptop with an Intel i7 CPU having 2.60GHz clock frequency and 16GB of RAM.

4.1. Reliability assessment

In the first set of numerical examples, we provide numerical evidence about the accuracy and well-balancing of the Split IMEX-RKC TG2-PC method.

4.1.1. Accuracy tests

In the first test, we simulate the viscous dam break problem without bed friction. We consider a uniform material height $H = 1 m$, a null initial condition for U_y , and an initial mass flux profile along the x -direction, given by

$$U_x(\mathbf{x}, 0) = \begin{cases} 1 & \text{if } x \leq L/2, \\ 0.5 & \text{if } x > L/2, \end{cases} \quad (30)$$

with $L = L_x = L_y = 5 m$. Here, we set the following simulation parameters $\rho = 1 \text{ kg/m}^3$, $\mu = 0.05 \text{ Pa}\cdot\text{s}$, $\tau_Y = 0 \text{ Pa}$, $T = 0.3 \text{ s}$, $g = 9.81 \text{ m/s}^2$.

In Fig. 3, we show the test results by gradually increasing the mesh refinement. In more detail, if l denotes the refinement level, the number of cells used to discretize the domain in both the x - and y -direction is equal to 2^l . Panels a), b) gather the analytical inviscid solution (in green) along the line $y = L_y/2$ (see panel c)) and at time T , together with the corresponding Split IMEX-RKC TG2-PC viscous solution (in black), when varying l from 5 to 11. The comparison is carried out in terms of the velocity component U_x (panel a)) and of the material height H (panel b)). As expected, the higher l , the sharper the approximation.

In a second test, we provide numerical evidence of the expected second-order convergence rate by considering a smooth configuration. We take into account the smoothly-varying domain identified by the orography profile

$$Z(r) = 1 + \frac{1}{10} \exp\left(-\frac{50}{L^2} r^2\right), \quad \text{with } r^2 = \left(x - \frac{L}{2}\right)^2 \quad (31)$$

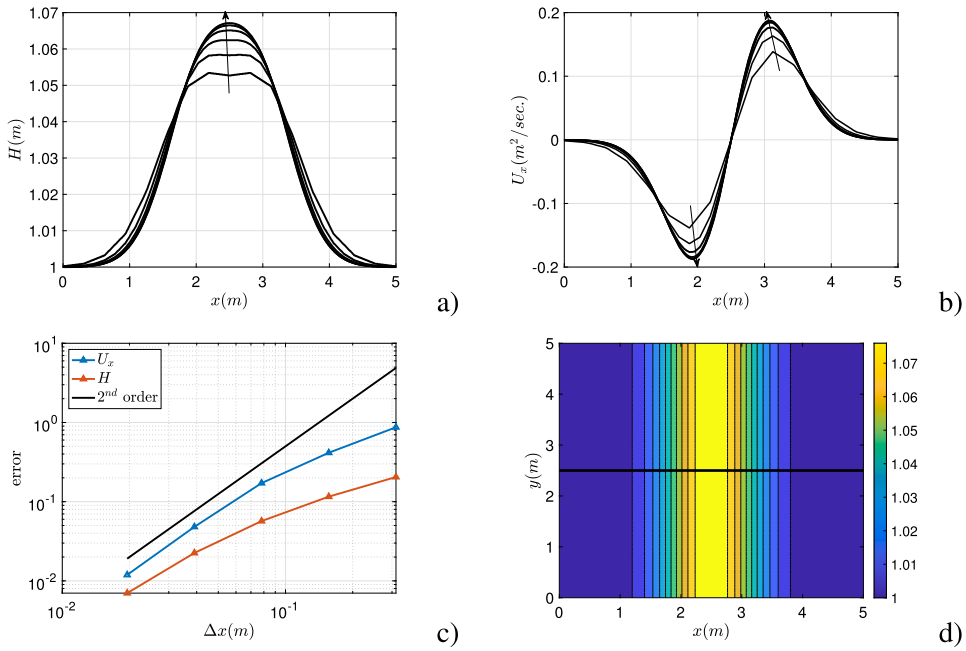


Fig. 4. Accuracy tests. Smooth solution. Panels a), b): solutions of the Split IMEX-RKC TG2-PC scheme for various levels of mesh refinement (the arrows highlight the increasing values of l); Panel c): convergence trend in $L^2(\Omega)$ -norm, where the reference solution refers to $l = 9$; Panel d): isolines of H for $l = 9$, with black-highlighted the line $y = L_y/2$ along which we compute the one-dimensional solution shown in panels a), b).

Table 1

Accuracy tests. Smooth solution. Number of stages of the RKC method (#stages RKC) for different values of l .

l	4	5	6	7	8	9
#stages RKC	2	3	4	6	9	12

and $L = L_x = L_y = 5$ m, and we set $\rho = 1$ kg/m³, $\mu = 0.5$ Pa·s, $\tau_Y = 0$ Pa, $T = 0.1$ s, $g = 9.81$ m/s². We assign a null initial mass flux and

$$H(r, 0) = Z(r) \quad (32)$$

as the initial material profile. We keep the CFL fixed at 0.9 in all the simulations. Finally, we consider a set of refinement levels from 4 to 9. In particular, the $L^2(\Omega)$ -norm of the error is computed with respect to the solution associated with the highest level (i.e., $l = 9$).

Fig. 4 gathers the results of such a convergence analysis. Panels a), b) provide the Split IMEX-RKC TG2-PC numerical solutions for the different refinement levels, computed along the line $y = L_y/2$ (see panel d)) and at time T . Panel c) displays the convergence trend of the error. We experience a sharp second-order convergence for the mass flux while the material height reaches a value of 1.68. In Table 1, we collect the number of RKC stages when increasing the number l of refinement levels.

Finally, in Fig. 5 we compare the Split IMEX-RKC TG2-PC scheme with the TG2 method when varying l from 4 to 8 (we refer to [6] for the specific TG2 scheme used for the comparison). We notice that the two approximate solutions approach each other when refining the mesh in accordance with the expectations. A comparison between the Split IMEX-RKC TG2-PC and the TG2 approaches will be carried out in terms of CPU time in Section 4.2.

4.1.2. Well-balancing test

This test problem aims to verify that the Split IMEX-RKC TG2-PC scheme maintains the well-balanced property over a non-flat bottom. With this aim, we consider the same configuration described in [54], namely a domain extension $L = L_x = L_y = 10$ m, a final time $T = 0.5$ s and two different functions to model the bottom orography, i.e.,

$$Z(\mathbf{x}) = Z_1(\mathbf{x}) = 5e^{-\frac{2}{5}(x-5)^2}, \quad (33)$$

which is smooth, and

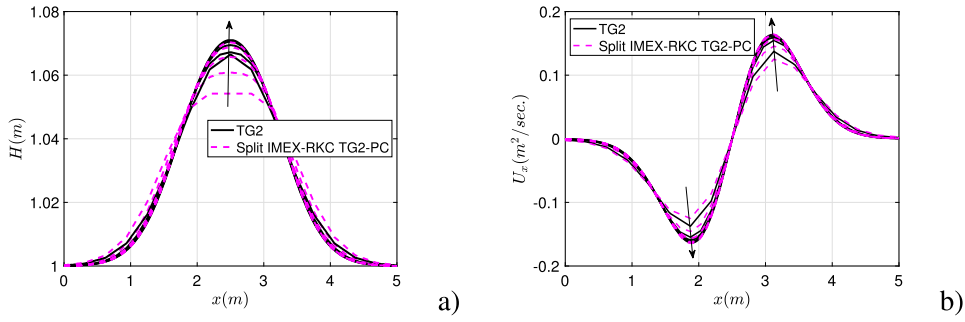


Fig. 5. Accuracy tests. Smooth solution. Panels a), b): comparison between the Split IMEX-RKC TG2-PC and the TG2 schemes for various levels of refinement, from 4 to 8.

Table 2

Well-balancing test. $L^1(\Omega)$ - and $L^\infty(\Omega)$ -norm of the error for the stationary solution in the presence of a smooth and of a discontinuous bed orography.

	$L^1(\Omega)$ -norm of the error			$L^\infty(\Omega)$ -norm of the error		
	H	U_x	U_y	H	U_x	U_y
Z_1	1.67e-13	4.87e-12	1.48e-12	8.88e-15	1.77e-13	1.21e-13
Z_2	1.54e-15	2.78e-13	1.52e-13	3.55e-15	4.48e-14	5.76e-14

$$Z(\mathbf{x}) = Z_2(\mathbf{x}) = \begin{cases} 4 & \text{if } 4 \leq x \leq 8 \\ 0 & \text{otherwise} \end{cases} \quad (34)$$

characterized by discontinuity. The initial condition coincides with the stationary solution,

$$H + Z(\mathbf{x}) = 10, \quad [U_x, U_y]^T = \mathbf{0}. \quad (35)$$

This steady-state configuration is expected to be preserved exactly by the numerical scheme. We consider a discretization of the domain with a level of refinement l equal to 8. Table 2 provides the $L^1(\Omega)$ - and $L^\infty(\Omega)$ -norm of the error associated with the two components of the velocity and the material height for both the considered orographies. All errors are close to the round-off independently of the selected bed profile, thus verifying the well-balancing property of the split IMEX-RKC TG2-PC method.

4.2. Efficiency assessment

In this section we verify the efficiency of the implementation of the Split IMEX-RKC TG2-PC scheme, by comparing the proposed method with the standard TG2 approach [4–6].

This analysis is performed on three case studies. In the first one, we consider a flat plane and a null yield shear stress τ_y , i.e., we deal with a Newtonian rheology; in the second test we still have a flat plane, but we consider bed friction with a Bingham fluid [31]; in the last configuration, we analyze the flow of a Bingham fluid with bed friction over an inclined plane orography. In the first example, we show the greater efficiency of the proposed Split IMEX-RKC TG2-PC scheme over the classical TG2 scheme, both in terms of time step selection and CPU time. Then, in the other two examples we provide strong scaling analyses that can be compared to the parallel performances experienced in the work [6] in the case of the TG2 scheme.

4.2.1. Example 1

We consider a flat and frictionless bed, a null yield shear stress, a final simulation time $T = 0.2$ s in a square domain with extension $L = L_x = L_y = 5$ m, for both the TG2 and Split IMEX-RKC TG2-PC schemes. We set null initial conditions on the mass fluxes, while selecting as initial material profile,

$$H(r, 0) = \begin{cases} 2 & \text{if } r \leq \frac{1}{2}, \\ 1 & \text{if } r > \frac{1}{2}, \end{cases} \quad (36)$$

where r is the radial distance from the barycenter of the square domain Ω , i.e., $r = \sqrt{(x - L/2)^2 + (y - L/2)^2}$. This is equivalent to considering a radial dam break problem with a gravitational field $g = 9.81$ m/s², a density $\rho = 1$ kg/m³ and a fluid viscosity $\mu = 0.1$ Pa·s.

Concerning the space discretization, at each time step, we resort to the same recovery-based mesh adaptation procedure as in [6], after setting a tolerance on the error estimator equal to $\tau = 10^{-5}$ m. The mesh adaptation process is constrained in terms of minimum resolution size along the x - and y -direction, which is set to $\{0.1, 0.05, 0.025, 0.0125\}$ m. We consider a CFL number equal to 0.9 and 1.8 for the TG2 and the Split IMEX-RKC TG2-PC method, respectively. We recall that such a number is calculated on the (whole)

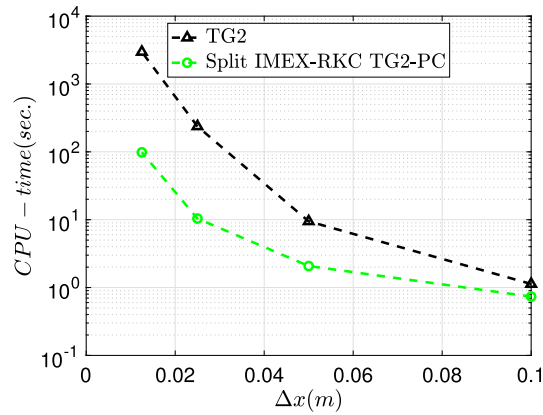


Fig. 6. Example 1. Plot of the CPU-time against the resolution Δx for both the TG2 and the Split IMEX-RKC TG2-PC methods (the y-axis is in semilogarithmic scale).

Table 3

Example 1. Time steps (in seconds) for the TG2 and the Split IMEX-RKC TG2-PC methods (second and third columns), number of stages required by the RKC method for the Split IMEX-RKC TG2-PC approach (fourth column), for the different minimum resolutions Δx considered (first column).

Δx	TG2	Split IMEX-RKC TG2-PC	#stages RKC
0.1	$6.86646 \cdot 10^{-3}$	$3.33623 \cdot 10^{-2}$	4
0.05	$1.71661 \cdot 10^{-3}$	$1.63593 \cdot 10^{-2}$	4
0.025	$4.29153 \cdot 10^{-4}$	$8.1052 \cdot 10^{-3}$	6
0.0125	$1.07288 \cdot 10^{-4}$	$4.05579 \cdot 10^{-3}$	8

time step Δt , while the first and third step of the Strang splitting adopt a time step equal to $\Delta t/2$. In this way, for the Split IMEX-RKC TG2-PC method, we recover a CFL number equal to 0.9 in the single TG2-PC procedure. Finally, the numerical simulations are carried out by using 4 processors.

We compare the TG2 and the Split IMEX-RKC TG2-PC approaches in terms of CPU-time (see Fig. 6) and the time step given by the CFL condition and the number of RKC stages (see Table 3), for the different minimum resolutions. We observe that the Split IMEX-RKC TG2-PC scheme enables the use of a considerably larger time step when compared with the TG2 method. This is corroborated by the CPU time. It is fully comparable for the largest resolution ($\Delta x = 0.1$ m), while it considerably reduces for the smallest resolution ($\Delta x = 0.0125$ m). Indeed, the CPU time required by the Split IMEX-RKC TG2-PC scheme is 3% of the one demanded by the standard TG2 scheme.

Finally, in panel a) of Fig. 7 we provide the adapted mesh at the final time, T , overlapped to the isolines of the material height H , when the minimum resolution is set to $\Delta x = 0.025$ m. Panel b) compares the TG2 and the Split IMEX-RKC TG2-PC methods by showing the mass flux U_x and the material height H distribution along the horizontal white line highlighted in panel a), when the minimum resolution is set to $\Delta x = 0.0125$ m. It is evident that the TG2 scheme is more dissipative with respect to the Split IMEX-RKC TG2-PC method. Thus, to improve the matching between the two approximations we have to employ a larger minimum resolution value and to decrease the CFL number. This is confirmed by the two bottom panels in the figure, which show also the Split IMEX-RKC TG2-PC solution for $\Delta x = 0.05$ m and a CFL number equal to 0.2.

4.2.2. Example 2

We consider the same configuration as in the previous section. We change the following simulation parameters, $\rho = 1300$ kg/m³, $\mu = 50$ Pa·s, and we consider a Bingham fluid with $\tau_Y = 10^3$ Pa.

In Fig. 8 we show some simulation results obtained with a level of refinement $l = 10$, which corresponds to a space resolution of roughly $5 \cdot 10^{-3}$ m in both directions. In particular, panels a), b) provide the trend of the material height and of the mass flux extracted along the x -direction at the final time T . The numerical scheme can detect both the rarefaction and the shock waves. Panels c), d) collect computational information, namely, the number of RKC stages against time and the speedup gained when increasing the number of processors from 16 to 512. We reach a parallel efficiency around 80%, even though we have over 300 RKC number of stages for all the simulation time. This confirms the efficiency of the implementation since the RKC method is a completely data-local method, and the number of RKC stages does not affect the parallel performances.

4.2.3. Example 3

This example involves a granular sliding mass along a planar orography profile so that the source term plays a role. The slope of the profile is approximately equal to 22° along the x axis. We choose the following parameters: gravitational field $g = 9.81$ m/s², simulation time $T = 5$ s, density $\rho = 1400$ kg/m³, viscosity $\mu = 50$ Pa·s, yield shear stress $\tau_Y = 2 \cdot 10^3$ Pa, turbulent coefficient

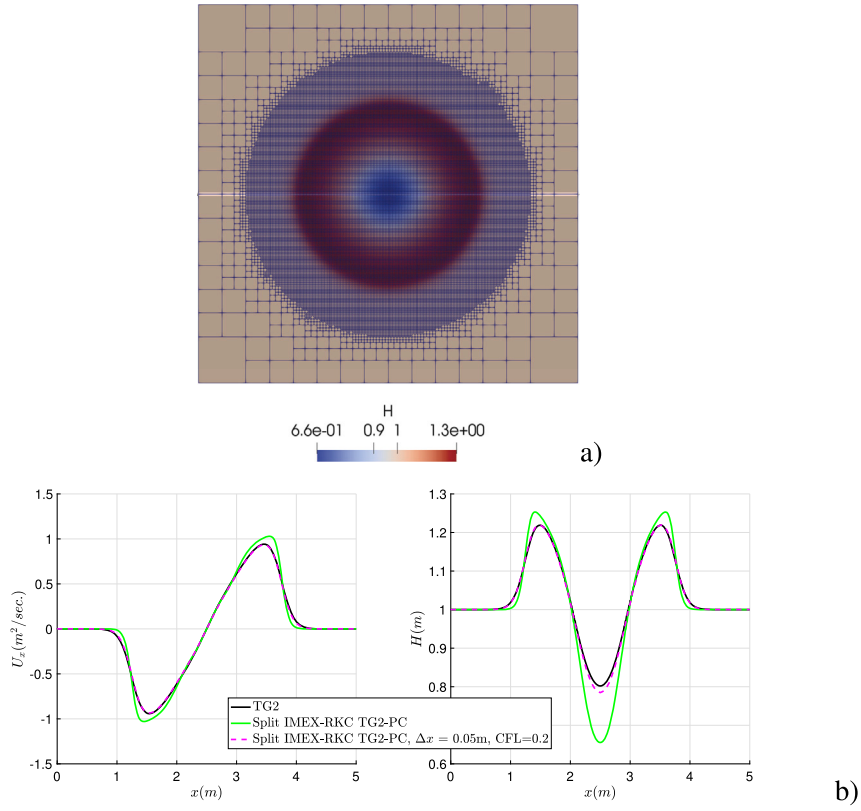


Fig. 7. Example 1. Panel a) shows the isolines of the material height overlapped to the adapted mesh at the final time T for $\Delta x = 0.025$ m; panel b) compares the approximation provided by the TG2 and the Split IMEX-RKC TG2-PC methods in terms of mass flux and material height distribution along the horizontal white line in panel a), for the finest minimum resolution value; the magenta dashed line tracks the Split IMEX-RKC TG2-PC solution for $\Delta x = 0.05$ m and a CFL number equal to 0.2.

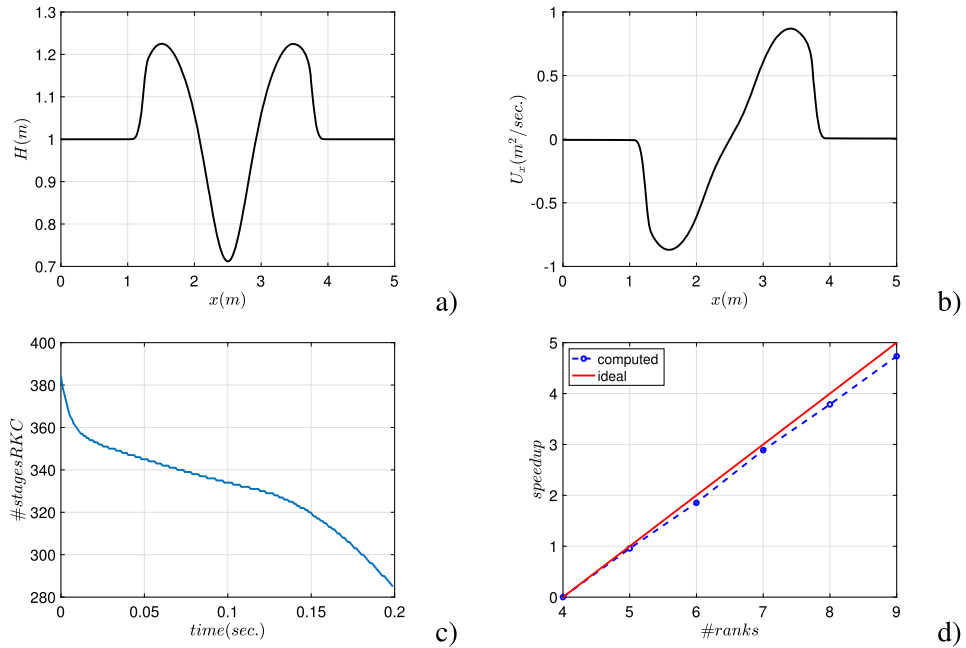


Fig. 8. Example 2. a) Material height and b) mass flux along the x -direction at the final time; c) RKC number of stages against time; d) speedup of the strong scaling analysis in a \log_2 - \log_2 plot.

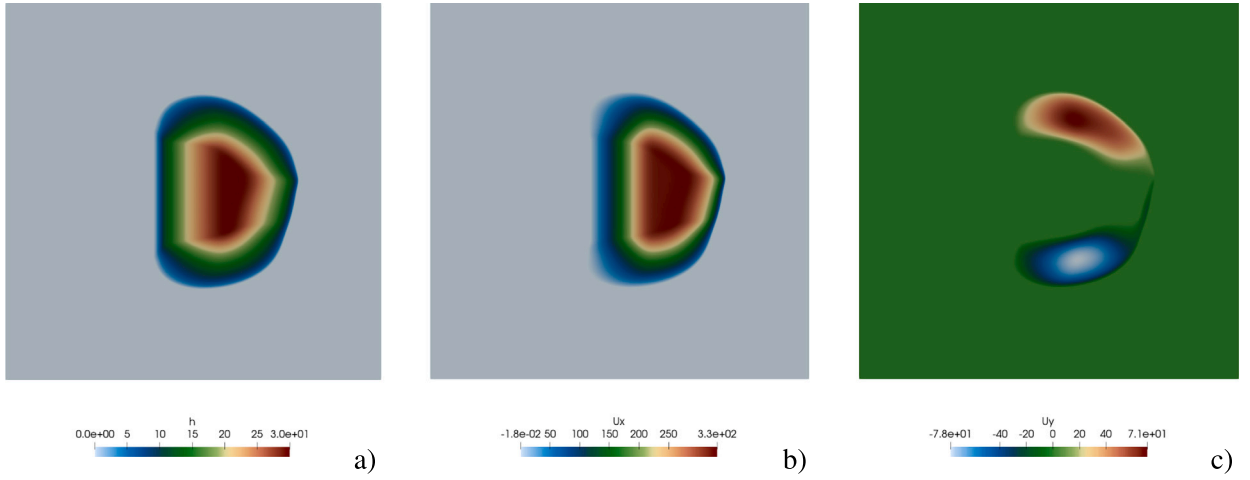


Fig. 9. Example 3. a) Material height, b) x- and c) y-direction mass flux distribution in Ω at the final time.

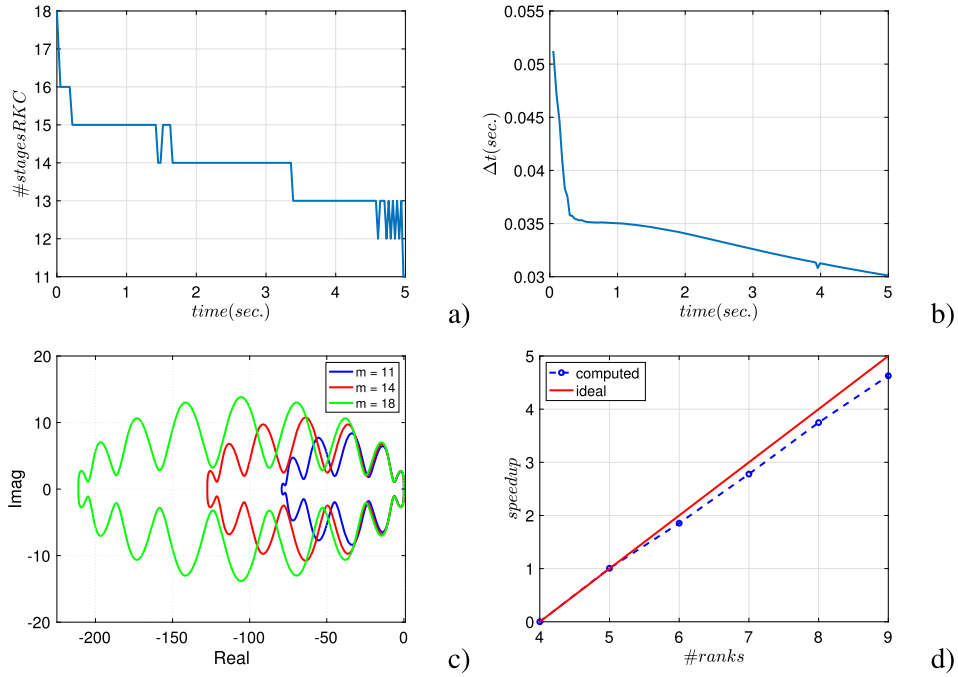


Fig. 10. Example 3. a) RKC number of stages against time; b) time step against time; c) absolute stability region for a different number m of stages; d) speedup of the scaling analysis in a log2-log2 plot.

$\xi = 10 \text{ m/s}^2$, bed friction angle $\delta = 23^\circ$, $p_S = 0 \text{ Pa}$, domain extension $L = L_x = L_y = 1000 \text{ m}$. We consider a material initially at rest, with an initial height

$$H(\mathbf{x}, 0) = \begin{cases} \max\{0, \min\{500x/L - 200, 30\}\} & \text{for } \mathbf{x} \in V, \\ 0 & \text{otherwise,} \end{cases} \quad (37)$$

where

$$V = \left\{ \mathbf{x} \in \mathbb{R}^2 : \frac{(x - L/2)^2}{L^2} + \frac{(y - L/2)^2}{L^2} \leq \left[0.2 + 0.01 \sin\left(10 \frac{y - L/2}{L} \frac{\pi}{L}\right) \right]^2 \right\}.$$

We adopt a space discretization with a level l of refinement equal to 10. Fig. 9 offers qualitative results of the simulation by providing the spatial distribution of the material height and of the x - and y -direction mass flux (from the left to the right panel) at time T . It is evident the absence of the slope contribution in panel c), while in panel b), we detect an offset due to the presence

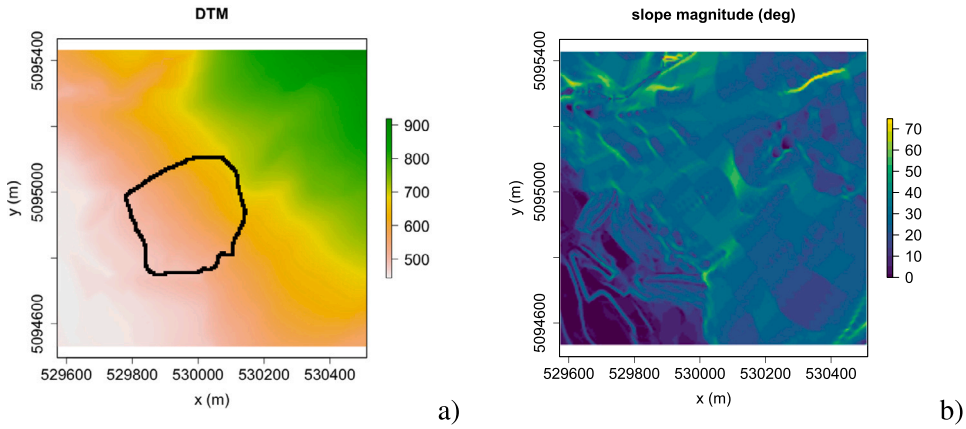


Fig. 11. Real case study. a) Isolines of the DTM together with its corresponding slope magnitude in degrees b).

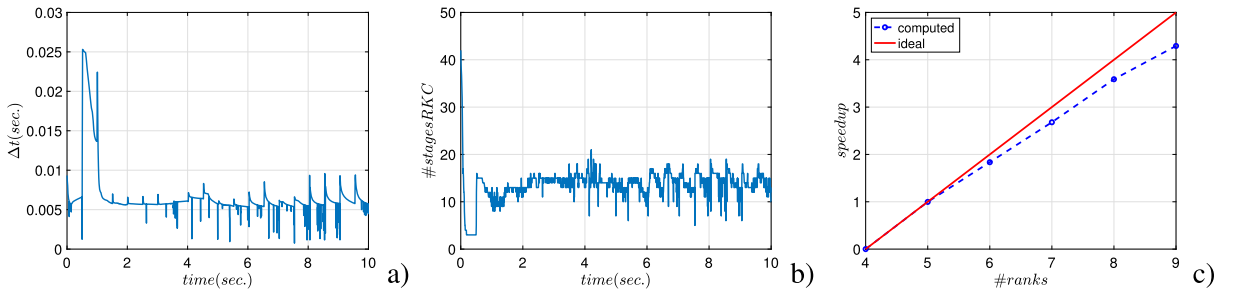


Fig. 12. Real case study. Evolution of a) the time step and b) of the RKC number of stages as a function of time; c) speedup of the scaling analysis in a \log_2 - \log_2 plot.

of the slope along the x -direction. Fig. 10 provides more quantitative information related to the numerical algorithm, namely the number of RKC stages against time in panel a), the time step size against time in panel b), the plot of the absolute stability region for three different numbers of stages in panel c), and the speedup of a strong scaling analysis using a number of processors from 16 to 512 in panel d). The RKC number of stages, as well as the time step, are decreasing during the simulation. This complies with the expectation since the problem is stiffer during the first movement of the material; then, the transport fluxes assume more importance leading to an advection-dominated setting. Panel c) highlights the increment of the stability region when increasing the value of m . We note that these stability regions are consistent with the ones in [23]. Such areas are computed by solving the following non-linear equation for the complex unknown z ,

$$|P_m(z)| = 1, \quad P_m(z) = 1 + b_m(T_m(\omega_0 + \omega_1 z) - T_m(\omega_0)).$$

Regarding the speedup, we obtain a parallel efficiency around 80%, analogously as for the previous test case.

4.3. A real case study

We focus now on a real case study simulation to show the capability of the Split IMEX-RKC TG2-PC method to deal with real problems. We will prove that the implemented algorithm ensures some strong scaling results when set in the space-time adaptive framework with quadtree interface tracking described in [6], where mesh adaptation is driven by material height.

We consider the Bindo-Corteno case study, namely a wide translational landslide, located in Valsassina (Lecco province, Lombardy, Italy) that underwent a catastrophic failure in December 2002 (volume ca $1.2 \cdot 10^6 \text{ m}^3$). We refer to [55] for a complete explanation of the involved geological aspects. The 5 m-resolution Digital Terrain Model (DTM) with domain extent $L_x = 820 \text{ m}$, $L_y = 870 \text{ m}$ is furnished, together with the corresponding slope, in Fig. 11, the mean slope angle being approximately equal to 28° . According to [56], the average thickness of the slide is assumed to be equal to 38 m, the material density is $\rho = 1291 \text{ kg/m}^3$, the bed friction angle is $\delta = 33.9^\circ$ and the surface pressure is $p_s = 1 \text{ atm}$. Regarding the Bingham and Voellmy rheological models, we set the following coefficients $\mu = 50 \text{ Pa}\cdot\text{s}$, $\tau_Y = 2 \cdot 10^3 \text{ Pa}$, $\xi = 10^3 \text{ m/s}^2$. We select a final time $T = 10 \text{ s}$, a cell resolution of 0.25 m in wet-dry interface regions, and a 1 m minimum resolution in wet regions. Finally, the space adaptation is carried out every 0.5 s, with a tolerance on the recovery-based estimator equal to $\tau = 10^{-5} \text{ m}$ (we refer to [6] for further details).

Fig. 12 shows the time evolution of the time step (panel a)) and of the number of stages of the RKC method (panel b)), together with the speedup characterizing the scaling analysis from 16 to 512 processors. The trend of Δt exhibits several peaks in correspondence with the spatial adaptation phases, although, on average, the behavior is very similar to the one in Fig. 10 where, after the

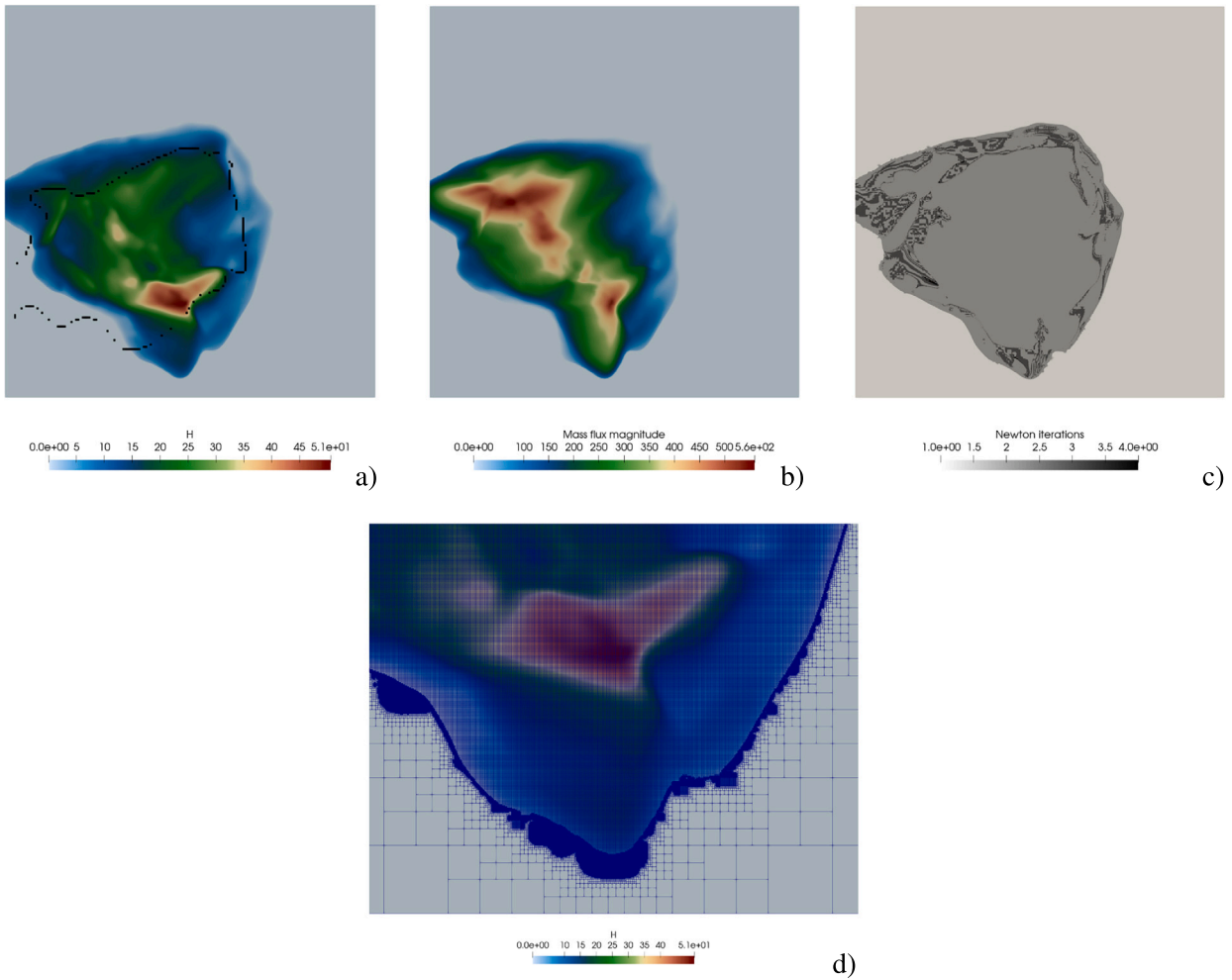


Fig. 13. Real case study. a) Material height and b) absolute value of the mass flux distribution at time T ; c) Newton iterations of the IMEX-RKC at the final stage and d) detail of the adapted mesh at time T .

initial movement of the material, the time step tends to reach a constant state when the landslide behaves similarly to a Newtonian fluid. The oscillatory plot of the time step finds a counterpart in the evolution characterizing the RKC number of stages. We note that the maximum number of mesh nodes is of the order of half a million. This results in a lower speedup (ranging between 60% and 70%) when compared with the cases presented in the previous sections.

Finally, in Fig. 13, we provide some sketches of the solution at the final time. In more detail, panel a) displays the material height colormap with, in black, the line representing the final landslide material deposition according to geological observations; panel b) provides the absolute value of the mass flux distribution; panel c) shows the isolines of the Newton iterations at the final stage of the RKC method; panel d) offers an enlarged view of the adapted mesh overlapped to the material height distribution. Panels a) and b) show that the landslide is reaching a steady state (as confirmed by the small values of $|U|$ along the falling mass boundary) in contrast to, for instance, the configuration in Fig. 9. This impacts the small number (up to 4) of iterations the Newton scheme demands to converge. Finally, we note the detection of the wet-dry interface guaranteed by the front-tracking methodology fully described in [6].

5. Conclusions

We have proposed an efficient parallel second-order well-balanced space-time numerical framework for simulating the run-out phase of rapid landslides.

The method is characterized by a larger stability region when compared with the standard TG2 scheme while preserving the locality of the implementation. The new method, which we name Split IMEX-RKC TG2-PC, combines the TG2-PC discretization with the IMEX-RKC approach through an operator-splitting strategy. We have applied the Split IMEX-RKC TG2-PC scheme to the solution of the single-phase depth-integrated model for fast-moving landslides and showed it to be exact when dealing with the lake-at-rest

steady state solution. In particular, the new numerical framework offers a more efficient tool when compared with the standard TG2 method in approximating the single-phase model for the run-out phase of fast-moving landslides.

The Split IMEX-RKC TG2-PC method has been numerically assessed in case of both idealized and real DTM orography configurations. In particular, after some reliability tests showing the accuracy and the numerical evidence of the well-balancing property of the numerical scheme, we have carried out some comparisons against the TG2 method in terms of time step selection and parallel performance and provided strong scaling results to show the efficiency of the parallel implementation.

As for possible future developments, we mention the possibility of exploiting the scalability of our code to perform simulation-intensive tasks such as an uncertainty quantification analysis applied to a real landslide run-out. This could be performed, for instance, by using methods like the polynomial chaos expansion [57]. We also plan to extend the proposed numerical simulation framework to include the landslide initiation phase dynamics. This implies the addition of the consolidation time process in the numerical model, which is the principal responsible of long-term landslide dynamics.

Data availability

Data will be made available on request.

Acknowledgements

This research was supported by the Accordo Attuativo ASI-POLIMI “Attività di Ricerca e Innovazione” n. 2018-5-HH.0.

C.d.F. and L.F. have been partially funded by the Italian Research Center on High-Performance Computing, Big Data and Quantum Computing (ICSC), European Union - Next Generation EU.

The present research is within the framework of the project “Dipartimento di Eccellenza 2023-2027” granted by Italian MUR.

We thank the anonymous reviewer for helping improve the manuscript’s quality.

References

- [1] J. Donea, A Taylor–Galerkin method for convective transport problems, *Int. J. Numer. Methods Eng.* 20 (1) (1984) 101–119.
- [2] R. Löhner, K. Morgan, O.C. Zienkiewicz, The solution of non-linear hyperbolic equation systems by the finite element method, *Int. J. Numer. Methods Fluids* 4 (11) (1984) 1043–1063.
- [3] B.V.K.S. Sai, O.C. Zienkiewicz, M.T. Manzari, P.R.M. Lyra, K. Morgan, General purpose versus special algorithms for high-speed flows with shocks, *Int. J. Numer. Methods Fluids* 27 (1–4) (1998) 57–80.
- [4] M. Quecedo, M. Pastor, A reappraisal of Taylor–Galerkin algorithm for drying–wetting areas in shallow water computations, *Int. J. Numer. Methods Fluids* 38 (6) (2002) 515–531.
- [5] M. Quecedo, M. Pastor, M.I. Herreros, J.A. Fernández Merodo, Numerical modelling of the propagation of fast landslides using the finite element method, *Int. J. Numer. Methods Eng.* 59 (6) (2004) 755–794.
- [6] F. Gatti, M. Fois, S. Perotto, C. de Falco, L. Formaggia, Parallel simulations for fast-moving landslides: space-time mesh adaptation and sharp tracking of the wetting front, *Int. J. Numer. Methods Fluids* 95 (8) (2023) 1286–1309.
- [7] G.I. Marchuk, Some application of splitting-up methods to the solution of mathematical physics problems, *Apl. Mat.* 13 (2) (1968) 103–132.
- [8] G. Strang, On the construction and comparison of difference schemes, *SIAM J. Numer. Anal.* 5 (3) (1968) 506–517.
- [9] G. Dal Maso, P.G. Lefloch, F. Murat, Definition and weak stability of nonconservative products, *J. Math. Pures Appl.* 74 (6) (1995) 483–548.
- [10] C. Parés, Numerical methods for nonconservative hyperbolic systems: a theoretical framework, *SIAM J. Numer. Anal.* 44 (1) (2006) 300–321.
- [11] M.J. Castro, E.D. Fernández-Nieto, A.M. Ferreiro, J.A. García-Rodríguez, C. Parés, High order extensions of Roe schemes for two-dimensional nonconservative hyperbolic systems, *J. Sci. Comput.* 39 (1) (2009) 67–114.
- [12] M. Castro, J.M. Gallardo, J.A. López-García, C. Parés, Well-balanced high order extensions of Godunov’s method for semilinear balance laws, *SIAM J. Numer. Anal.* 46 (2) (2008) 1012–1039.
- [13] J.M. Gallardo, C. Parés, M. Castro, On a well-balanced high-order finite volume scheme for shallow water equations with topography and dry areas, *J. Comput. Phys.* 227 (1) (2007) 574–601.
- [14] M.L. Muñoz-Ruiz, C. Parés, Godunov method for nonconservative hyperbolic systems, *ESAIM: Math. Model. Numer. Anal.* 41 (1) (2007) 169–185.
- [15] M. Castro, A. Pardo, C. Parés, E. Toro, On some fast well-balanced first order solvers for nonconservative systems, *Math. Comput.* 79 (271) (2010) 1427–1472.
- [16] M. Dumbser, M. Castro, C. Parés, E.F. Toro, Ader schemes on unstructured meshes for nonconservative hyperbolic systems: applications to geophysical flows, *Comput. Fluids* 38 (9) (2009) 1731–1748.
- [17] M. Dumbser, D.S. Balsara, A new efficient formulation of the hllm Riemann solver for general conservative and non-conservative hyperbolic systems, *J. Comput. Phys.* 304 (2016) 275–319.
- [18] M. Dumbser, A. Hidalgo, M. Castro, C. Parés, E.F. Toro, Force schemes on unstructured meshes II: non-conservative hyperbolic systems, *Comput. Methods Appl. Mech. Eng.* 199 (9–12) (2010) 625–647.
- [19] M. Castro, J. Gallardo, C. Parés, High order finite volume schemes based on reconstruction of states for solving hyperbolic systems with nonconservative products. Applications to shallow-water systems, *Math. Comput.* 75 (255) (2006) 1103–1134.
- [20] M. Dumbser, E.F. Toro, A simple extension of the Osher Riemann solver to non-conservative hyperbolic systems, *J. Sci. Comput.* 48 (1) (2011) 70–88.
- [21] F. Fambri, M. Dumbser, S. Köppel, L. Rezzolla, O. Zanotti, Ader discontinuous Galerkin schemes for general-relativistic ideal magnetohydrodynamics, *Mon. Not. R. Astron. Soc.* 477 (4) (2018) 4543–4564.
- [22] S. Busto, M. Dumbser, S. Gavrilyuk, K. Ivanova, On thermodynamically compatible finite volume methods and path-conservative ader discontinuous Galerkin schemes for turbulent shallow water flows, *J. Sci. Comput.* 88 (1) (2021) 28.
- [23] J.G. Verwer, B.P. Sommeijer, An implicit-explicit Runge-Kutta-Chebyshev scheme for diffusion-reaction equations, *SIAM J. Sci. Comput.* 25 (5) (2004) 1824–1835.
- [24] J.G. Verwer, W. Hundsdorfer, B.P. Sommeijer, Convergence properties of the Runge-Kutta-Chebyshev method, *Numer. Math.* 57 (1) (1990) 157–178.
- [25] B.P. Sommeijer, L.F. Shampine, J.G. Verwer, RKC: an explicit solver for parabolic PDEs, *J. Comput. Appl. Math.* 88 (2) (1998) 315–326.
- [26] R. Bermejo, J. Carpio, An adaptive finite element semi-Lagrangian implicit–explicit Runge–Kutta–Chebyshev method for convection dominated reaction–diffusion problems, *Appl. Numer. Math.* 58 (1) (2008) 16–39.

- [27] R. Bermejo, P.G. del Sastre, An implicit-explicit Runge-Kutta-Chebyshev finite element method for the nonlinear lithium-ion battery equations, *Appl. Math. Comput.* 361 (2019) 398–420.
- [28] M.B. Abbott, *Computational Hydraulics: Elements of the Theory of Free Surface Flows*, Pitman, London, 1979.
- [29] A. Franci, M. Cremonesi, U. Perego, G. Crosta, E. Oñate, 3D simulation of Vajont disaster. Part 1: numerical formulation and validation, *Eng. Geol.* 279 (2020) 105854.
- [30] M. Pastor, T. Blanc, B. Haddad, V. Drempeit, M. Mories, P. Stickle, M. Mira, J. Merodo, Depth averaged models for fast landslide propagation: mathematical, rheological and numerical aspects, *Arch. Comput. Methods Eng.* 22 (2015) 67–104.
- [31] T.C. Papanastasiou, Flows of materials with yield, *J. Rheol.* 31 (5) (1987) 385–404.
- [32] A. Franci, M. Cremonesi, U. Perego, E. Oñate, G. Crosta, 3D simulation of Vajont disaster. Part 2: multi-failure scenarios, *Eng. Geol.* 279 (2020) 105856.
- [33] R.J. LeVeque, Balancing source terms and flux gradients in high-resolution Godunov methods: the quasi-steady wave-propagation algorithm, *J. Comput. Phys.* 146 (1) (1998) 346–365.
- [34] O. Gourgue, R. Comblen, J. Lambrechts, T. Kärnä, V. Legat, E. Deleersnijder, A flux-limiting wetting–drying method for finite-element shallow-water models, with application to the Scheldt estuary, *Adv. Water Resour.* 32 (12) (2009) 1726–1739.
- [35] J. Qiu, M. Dumbser, C.-W. Shu, The discontinuous Galerkin method with Lax–Wendroff type time discretizations, *Comput. Methods Appl. Mech. Eng.* 194 (42–44) (2005) 4528–4543.
- [36] M. Pastor, M. Quecedo, J. Fernández Merodo, M. Herrores, E. Gonzalez, P. Mira, Modelling tailings dams and mine waste dumps failures, *Geotechnique* 52 (8) (2002) 579–591.
- [37] D. Givoli, Non-reflecting boundary conditions, *J. Comput. Phys.* 94 (1) (1991) 1–29.
- [38] O.C. Zienkiewicz, K. Morgan, *Finite Elements and Approximation*, Courier Corporation, 2006.
- [39] M.J. Castro, P.G. LeFloch, M.L. Muñoz-Ruiz, C. Parés, Why many theories of shock waves are necessary: convergence error in formally path-consistent schemes, *J. Comput. Phys.* 227 (17) (2008) 8107–8129.
- [40] S. Rhebergen, O. Bokhove, J.J. van der Vegt, Discontinuous Galerkin finite element methods for hyperbolic nonconservative partial differential equations, *J. Comput. Phys.* 227 (3) (2008) 1887–1922.
- [41] R. Abgrall, S. Karni, A comment on the computation of non-conservative products, *J. Comput. Phys.* 229 (8) (2010) 2759–2763.
- [42] J. Peraire, A finite element method for convection dominated flows, Ph.D. thesis, University College of Swansea, Swansea, 1986.
- [43] S.T. Zalesak, Fully multidimensional flux-corrected transport algorithms for fluids, *J. Comput. Phys.* 31 (3) (1979) 335–362.
- [44] J.P. Boris, D.L. Book, Flux-corrected transport. III. Minimal-error FCT algorithms, *J. Comput. Phys.* 20 (4) (1976) 397–431.
- [45] D. Kuzmin, M. Möller, S. Turek, High-resolution FEM–FCT schemes for multidimensional conservation laws, *Comput. Methods Appl. Mech. Eng.* 193 (45–47) (2004) 4915–4946.
- [46] Y. Xing, X. Zhang, C.-W. Shu, Positivity-preserving high order well-balanced discontinuous Galerkin methods for the shallow water equations, *Adv. Water Resour.* 33 (12) (2010) 1476–1493.
- [47] J.G. Verwer, Explicit Runge-Kutta methods for parabolic partial differential equations, *Appl. Numer. Math.* 22 (1–3) (1996) 359–379.
- [48] B. Wohlmuth, Variationally consistent discretization schemes and numerical algorithms for contact problems, *Acta Numer.* 20 (2011) 569–734.
- [49] R.L. Berge, I. Berre, E. Keilegavlen, J.M. Nordbotten, B. Wohlmuth, Finite volume discretization for poroelastic media with fractures modeled by contact mechanics, *Int. J. Numer. Methods Eng.* 121 (4) (2020) 644–663.
- [50] L. Formaggia, F. Gatti, S. Zonca, An XFEM/DG approach for fluid-structure interaction problems with contact, *Appl. Math.* 66 (2) (2021) 183–211.
- [51] P.C. Africa, Scalable adaptive simulation of organic thin-film transistors, PhD Thesis in: Mathematical Models and Methods in Engineering, Politecnico di Milano, Milano, Italy, 2019.
- [52] P.C. Africa, C. de Falco, S. Perotto, Scalable recovery-based adaptation on Cartesian quadtree meshes for advection-diffusion-reaction problems, *Adv. Comput. Sci. Eng.* 1 (4) (2023) 443–473.
- [53] C. Burstedde, L.C. Wilcox, O. Ghattas, p4est: scalable algorithms for parallel adaptive mesh refinement on forests of octrees, *SIAM J. Sci. Comput.* 33 (3) (2011) 1103–1133.
- [54] Y. Xing, C.-W. Shu, A new approach of high order well-balanced finite volume WENO schemes and discontinuous Galerkin methods for a class of hyperbolic systems with source terms, *Comput. Phys.* 1 (1) (2006) 100–134.
- [55] C. Margottini, P. Canuti, K. Sassa, *Landslide Science and Practice: Volume 3: Spatial Analysis and Modelling*, vol. 3, Springer Science & Business Media, 2013.
- [56] M.M. Secondi, G. Crosta, C. di Prisco, G. Frigerio, P. Frattini, F. Agliardi, Landslide motion forecasting by a dynamic visco-plastic model, in: *Landslide Science and Practice*, Springer, 2013, pp. 151–159.
- [57] B. Sudret, Global sensitivity analysis using polynomial chaos expansions, *Reliab. Eng. Syst. Saf.* 93 (7) (2008) 964–979.